https://doi.org/10.5194/egusphere-2026-1662
Preprint. Discussion started: 26 March 2026

Empirical evidence of overestimated Ku-band sea ice radar freeboards in satellite altimetry

Catherine Taelman[1], Jack C. Landy[1], Robbie D.C. Mallett[1], and Polona Itkin[2]

[1]UiT The Arctic University of Norway, Tromsø, Norway
[2]the Norwegian Polar Institute, Tromsø, Norway

Correspondence: Catherine Taelman (catherine.c.taelman@uit.no)

Abstract. Pan-Arctic sea ice thickness estimates are routinely produced from Ku-band radar altimetry observations. State-of-the-art waveform retracking algorithms rely on the uncertain assumption that Ku-band radar waves penetrate through the snow and that the dominant return originates from surface scattering at the snow/ice interface. However, growing evidence suggests that Ku-band radar altimetry freeboards may not always accurately track this elevation. We investigate this question by analyzing the evolution of spaceborne radar and laser freeboards over immobile regions of landfast first-year ice (FYI) and multi-year ice (MYI) off Greenland's coast from mid-winter to mid-summer 2022. Our results suggest that the radar freeboards over FYI trace the snow/ice interface during most of the cold season (up to mid-May, at this location), providing empirical support for the validity of the assumption of full snow penetration at Ku-band frequency. Over MYI, the retracked heights correspond to locations well below the air/snow interface most of the time, at least 60% deep in the snow, but the exact depth could not be reliably assessed. However, these data also provide evidence for a positive bias in Ku-band radar freeboards during short intervals throughout the winter and the melt season, for both ice types. In particular, our results suggest that, during winter, the Ku-band radar freeboards tend to be biased high: i) for ice with a saline snow cover during a warming event (brine volume$>$1%), and ii) during and immediately after strong snowfall events. Winter warming events are often accompanied by snowfall, leading to a cumulative bias for the areas with saline snow - i.e. most FYI in the Arctic. In the period of snow melt onset in May/June, biased radar freeboards appear to be related to saline snow only, but biases are on average larger (up to 10 cm) than during the winter period (under 4 cm). Though our results indicate a positive bias in satellite radar freeboards under specific snow conditions, periods of biased freeboard are short-term during the winter - in total accounting for approximately 15% of the time. Our findings therefore generally support the assumption of full snow penetration for Ku-band sea ice thickness and dual-altimetry snow depth retrievals during winter, such as planned for the Copernicus Polar Ice and Snow Topography Altimeter (CRISTAL) mission.

https://doi.org/10.5194/egusphere-2026-1662
Preprint. Discussion started: 26 March 2026

1 Introduction

Spaceborne laser and radar altimetry observations have provided a consistent record of Arctic basin-wide autumn-spring sea ice thickness (SIT) estimates for the last two decades (Kacimi and Kwok, 2024). Recent advancements in the processing algorithms now also provide SIT estimates in the melt period (Landy et al., 2022). Altimeters, however, do not directly observe ice thickness, but rather provide an estimate of the ice freeboard (FB_i), which is the height of the floating ice above the sea surface. The ice freeboard is then converted to ice thickness through Archimedes' principle (Laxon et al., 2003). State-of-the-art algorithms estimate ice freeboard from either laser or Ku-band radar observations. Laser altimeters, such as onboard the polar-orbiting ICESat-2 mission, measure the laser freeboard (sometimes called the total freeboard), which equals the ice freeboard plus any overlying snow cover (Kwok et al., 2004). It is generally assumed that the laser does not significantly penetrate into the snow and hence returns mainly originate from the air/snow interface (Kwok et al., 2004). On the other hand, pulses from radar altimeters operating at Ku-band frequency, such as onboard the CryoSat-2 and Sentinel-3 missions, can penetrate into the snow cover (Kacimi and Kwok, 2024; Fredensborg Hansen et al., 2024). Correctly interpreting radar altimetry waveform returns over sea ice requires understanding how the radar waves interact with the snow layer and underlying ice. Radar altimeters provide measurements of the radar freeboard, which we define here as the height of the principal backscatter response from the snow/sea ice interface relative to the local instantaneous sea surface height (Ricker et al., 2014). This is an idealized assumption, so the derived radar freeboard can be biased if the principal backscatter response does not originate from this interface.

State-of-the-art algorithms used in the production of pan-Arctic SIT estimates assume that the main Ku-band radar return originates from the snow/ice interface (Laxon et al., 2003, 2013). This assumption may hold for cold, dry, brine-free, and homogeneous snowpacks over smooth ice, as supported by the laboratory experiment of (Beaven et al., 1995) - albeit with a very different radar sensing geometry than is used from space. However, more recent studies have suggested that natural variations in physical snow properties can result in dielectric snow properties that significantly alter radar scattering and absorption at the interfaces and/or within the snow volume. Among others, the following snow properties have been shown to impact the snow dielectric properties in the microwave spectrum: temperature, density, salinity, liquid water content, grain morphology, and metamorphic features (Barber et al., 1995; Willatt et al., 2011; Ricker et al., 2015; Nandan et al., 2017; Rösel et al., 2020; Nandan et al., 2020; Tonboe et al., 2021; Jutila and Haas, 2023).

Increased microwave backscattering and attenuation by the snow could result in an upward shift of the radar backscatter height distribution relative to the snow/ice interface, leading to overestimated radar freeboards if no additional competing biases are present (Nandan et al., 2017; Rösel et al., 2020). This assumes the dominant backscatter mechanism transfers from surface scattering at the snow/ice interface to internal snowpack volume scattering. However, surface-based studies have generally found that Ku-band radar returns are often multi-peaked, with dominant returns originating from surface scattering at the air/snow and snow/ice interfaces, and relatively little power returning from between. The relative contribution of each interface depends on the snow physical properties, such as density, hardness and snow surface topography (Stroeve et al., 2020; Landy et al., 2020; Nandan et al., 2023; Willatt et al., 2023). At airborne scales, De Rijke-Thomas et al. (2023) argue that strong, quasi-specular scattering is the main mechanism contributing to the radar returns and that the return power from the snow/ice

https://doi.org/10.5194/egusphere-2026-1662
Preprint. Discussion started: 26 March 2026

interface is on average 3–5 times larger than from the air/snow interface for FYI. At satellite scales, however, individual returns from the air/snow and snow/ice interfaces cannot typically be differentiated due to the ∼47 cm range resolution of the radar altimeters onboard CS-2 and S-3 (Kwok, 2014).

The detected waveform at the CS-2/S-3 footprint scale is a signal composed of the cumulative contributions from surface scattering at all scattering interfaces plus potentially snow volume scattering, modulated by the height distribution of the sea ice topography. If the relative contribution of the snow/ice interface is not dominant compared to the other contributions, the retracked height might not represent the location of the snow/ice interface but rather a location higher up in the snow. The dominant radar backscatter may not actually originate from within the snow - multiple strong, peaked echoes from different scattering surfaces may be detected as a merged waveform with a height retracked between the scattering surfaces. Results from waveform modeling studies back this up; suggesting that snow microstructure properties are relatively unimportant compared to the multi-scale roughness and dielectric contrast between interfaces (Tonboe et al., 2021; Landy et al.). Still, snow volume scattering can be significant when the snow layering is complex or the snow depth is thick, as is typically the case for Antarctic snow packs (Willatt et al., 2025; Zhou et al., 2026). A few studies report satellite-based empirical observations of biases between retracked radar freeboards and the (expected) location of the snow/ice interface (Ricker et al., 2015; King et al., 2018; Nab et al., 2023). In Ricker et al. (2015) the authors report a positive correlation between snow freeboards from buoys and radar freeboards from CS-2 over periods with substantial snow depth changes. Similar findings are reported in Nab et al. (2023), where the authors show that satellite Ku-band radar freeboards are, paradoxically, often positively correlated to snow accumulation on short timescales.

Snow covers on FYI are typically characterized by a saline bottom layer due to upwards brine transport from the ice or (more rarely in the Arctic) surface flooding (Nandan et al., 2017; Rösel et al., 2020). The presence of salt depresses the freezing point and introduces liquid water in the snowpack at temperatures below 0°C, with knock-on impacts on microwave permittivity. Results from theoretical models parameterized with in situ observations from Arctic field campaigns have suggested that saline snow could bias Ku-band radar freeboards up to ∼7 centimeters high (Nandan et al., 2017, 2020; Tonboe et al., 2021). Coarse temporal sampling and a lack of auxiliary snow information have prevented this effect from being observed directly from space, though there is some evidence for overestimated Ku-band radar freeboards in airborne radar observations of FYI (King et al., 2018; Rösel et al., 2020).

An outstanding hurdle preventing full understanding of the impacts of snow for Ku-band radar altimetry freeboard measurements is the lack of continuous satellite observations over the same ice floe over time. Sea ice typically drifts many 10s kilometers between the ∼monthly sampling interval of repeat nadir-looking altimeter passes. The seasonal evolution of space-borne radar waveform parameters and freeboards has therefore only therefore studied on a statistical basis at around monthly resolution (Khvorostovsky et al.) or in detailed surface-based studies (Stroeve et al., 2020). Here, we aim to investigate the seasonal evolution of satellite radar altimetry observations over the same sea ice from mid-winter to mid-summer. We track how the ice and its snow cover evolve under changing atmospheric conditions, considering areas of FYI and MYI separately. Over FYI the time series covers the entire cycle of ice formation, ice growth and snow accumulation, and eventually melt. This allows us to evaluate the impact of ice type, snow surface roughness, snow accumulation, and physical snow property changes

https://doi.org/10.5194/egusphere-2026-1662
Preprint. Discussion started: 26 March 2026

on the retrieved freeboards, in a controlled manner. Of particular interest is the interaction of radar waves at the Ku-band frequency with snow on FYI. We:

1. identify immobile regions of FYI and MYI in C-band synthetic aperture radar (SAR) imagery that can be tracked from mid-winter to mid-summer. The FYI regions are outlined such that they include the full seasonal cycle from the day of ice formation, through snow accumulation and ice growth, and eventually melt. We then retrieve coinciding laser and radar satellite altimetry measurements from ICESat-2, CryoSat-2, and Sentinel-3 over these regions.

2. observe the derived principal laser and Ku-band radar backscatter elevations over the seasonal cycle, with respect to the local sea level. We analyze the impact of changing atmospheric conditions on the retracked elevations and relate the satellite-derived time series to in situ measurements, as well as radar modeling and snow/ice modeling results.

3. investigate whether there is a bias between the retracked heights derived at Ku-band frequency and the location of the snow/ice interface. Based on the results of previous studies, we test the hypothesis that 1) saline snow on FYI can bias the radar freeboards high, especially when snow temperatures approach the melting point, and 2) radar freeboards can be biased high during and immediately after snowfall. We consider the implications for downstream geophysical products such as dual-frequency snow depth and sea ice thickness estimates.

This paper is structured as follows: Section 2 introduces the study area, and Sections 3 and 4 the data and methods of this study, respectively. Results are presented in Section 5 and discussed in Section 6. Finally, we emphasize the main findings in the conclusion.

2 Study Area

This study focuses on the geographical area of Belgica Bank, which is located off the northeast coast of Greenland. A vast amount of immobile landfast ice, known as the Norske Øer Ice Barrier, forms every year above the bank and is therefore an ideal study site to investigate satellite returns from the same sea ice over an entire seasonal cycle (Hughes et al., 2011). Belgica Bank is a very shallow part of the northeast continental shelf of Greenland between 78–80°North and 12–16°West. Landfast ice easily forms here due to the grounding of icebergs and ridge keels in the shallow waters. These grounding points serve as anchors for drifting ice (Hughes et al., 2011). As a result, the fast ice can extend up to 200 kilometers away from the Greenlandic coast. The eastern edge of the Ice Barrier borders drifting ice that is transported through the Fram Strait by the East Greenland Current and, as such, there are regular open water areas adjacent to the fast ice edge that constrain the local sea surface height and allow valid altimeter freeboard measurements to be made. Typical ice conditions in the Øer Ice Barrier include a mixture of multi-year ice (MYI) exported through Fram Strait and young and first-year ice (FYI) forming locally (Hughes et al., 2011; Lohse et al., 2024). The ice cover is therefore varied in ice age, surface roughness, and weather history.

https://doi.org/10.5194/egusphere-2026-1662
Preprint. Discussion started: 26 March 2026

2.1 Selection of ROIs

The stationary nature of fast ice has two main advantages: 1) it is possible to gather and compare remote sensing observations over the exact same ice from a range of different sensors over several seasons, and 2) new ice can be assumed to be predominantly grow in a thermodynamic way. Here, we defined two sets of regions of interest (ROIs): one including areas of level FYI that formed locally, and another including areas of older, deformed ice. The ROIs were manually outlined by visual interpretation of C-band SAR imagery, where smooth ice appears relatively dark while deformed ice looks significantly brighter. We gathered a time series of SAR imagery over the Øer Ice Barrier between October 2021 and August 2022 to get an overview of the ice conditions throughout the season and to guide us in the selection of suitable ROIs. Careful attention was paid to finding areas where the ice is completely immobile during the entire season, to avoid needing drift correction. Furthermore, we only selected areas up to ∼50 km away from the Ice Barrier's eastern edge to ensure the presence of nearby sea surface reference samples required for freeboard retrievals. Lastly, the ROIs were outlined such that the ice surface within a ROI appears homogeneous in the SAR imagery and it is thus reasonable to assume that any altimetry track crossing the ROI provides a representative sample of the ice class.

All ROIs selected for the FYI class formed in situ in the Øer Ice Barrier within the span of 4 weeks in January–February 2022 and stayed in place well into the melt season without experiencing significant deformation. This implies that all FYI ROIs underwent the full seasonal cycle which includes ice formation, snow accumulation and ice growth, and eventually melt or breakup. These ROIs thus capture the evolution from new ice to FYI. The class consisting of older, deformed ice generally contains areas with a mixture of heavily deformed MYI that was advected from the north and a smaller fraction of FYI that formed locally and was crushed in between the larger MYI floes. We refer to this as the MYI class in the remainder of this paper, as the ice in these areas predominantly has the characteristics of MYI and hence results are representative for Arctic MYI. For consistency, we chose to identify MYI ROIs that can be tracked throughout the same time period as the FYI. A total of 12 FYI and 6 MYI ROIs were outlined in this way, covering areas in the range 15–950 km^2, as shown in Fig. 1. All ROIs form or start being immobile between 25 January–22 February and break up between 15 May–8 August 2022.

3 Data

3.1 SAR

We gathered a time series of C-band SAR imagery over the Øer Ice Barrier study area (outlined in Fig. 1) between October 2021 and August 2022. We used SAR images acquired by the Sentinel-1 (S-1) satellites from ESA, which image at C-band (5.405 GHz). All S-1 scenes used here were acquired in Extra Wide (EW) swath mode, which corresponds to a swath width of approximately 410 kilometers. This mode images in dual-polarization (HH and HV) with incidence angles in the range 18.9–47°. The products were collected from the Copernicus Data Space Ecosystem in Ground Range Detected Medium resolution (GRDM) format, which has a spatial resolution of 93×87 m (range-azimuth). The failure of Sentinel-1B in December 2021

https://doi.org/10.5194/egusphere-2026-1662
Preprint. Discussion started: 26 March 2026

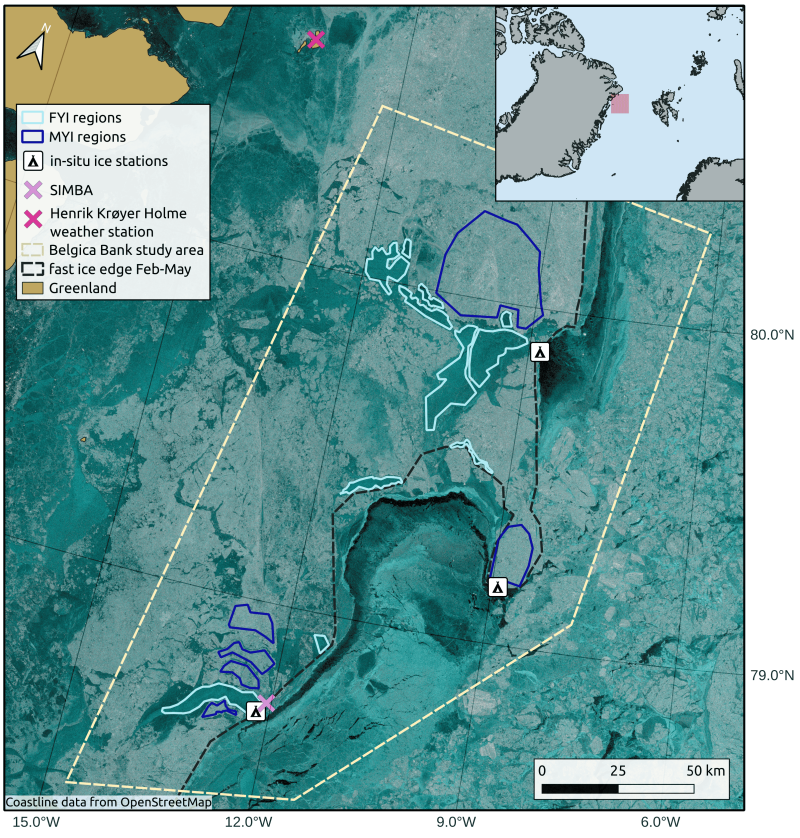

Figure 1. Overview map showing the FYI and MYI ROIs, in situ ice stations, and weather station in the Øer Ice Barrier area. The background is a Sentinel-1 false-color SAR image acquired on 28 April 2022 to illustrate the ice conditions at the time of the study. The fast ice edge outlined on the map shows the minimum fast ice extent for the months January–May 2022, hence it does not exactly match with the fast ice edge of the background SAR image.

led to a lower temporal resolution during the time of the study, but nevertheless there were on average two image acquisitions per day over the study area, resulting in a SAR time series of 366 images between January and August 2022.

3.2 Altimetry

After outlining the ROIs in the SAR imagery, we collected laser and radar altimetry data that covered the Øer Ice Barrier study area between January and August 2022.

3.2.1 Laser altimetry

The Ice, Cloud, and land Elevation Satellite-2 (ICESat-2, hereafter referred to as IS-2) laser altimetry mission from NASA carries onboard the Advanced Topographic Laser Altimeter System (ATLAS). ATLAS is a photon-counting lidar operating at

https://doi.org/10.5194/egusphere-2026-1662
Preprint. Discussion started: 26 March 2026

a 524 nm wavelength and providing surface height measurements across six different beams. The six beams are organized in pairs and one pair consists of a weak and a strong beam. The laser has a pulse repetition frequency of 10 kHz, which results in the ∼ 17m (diameter) footprints being ∼ 0.7m apart in along-track direction. The satellite provides coverage up to 88°North.

We use the IS-2 ATL07 and ATL10 sea ice products. ATL07 contains along-track surface heights per track, provided in segments that corresponds to ∼150 photon aggregates. This means that the length of segments is not fixed but rather varies with surface type, i.e. a highly reflective surface will yield a shorter segment. As a result the ALT10 freeboard estimates come in varied along-track resolution (Kwok et al., 2021). The ATL10 product provides freeboard estimates per track, based on the ATL07 surface heights, where segments classified as *sea surface* provide reference sea surface tie points. Freeboard here means the total ice and snow freeboard. Note that the ATL10 product is only provided for areas with an ice concentration above 50% and more than 25 km distance from land (Kwok et al., 2021), and that observations can be hindered by clouds. Furthermore, freeboard is only calculated when at least one *sea surface* reference point is available within 10 kilometers distance along the same track. We used release 006 (r006) ATL07 and ATL10 data accessed through the National Snow and Ice Data Center (NSIDC) DAAC (Kwok et al., 2023).

3.2.2 Radar altimetry

We used radar altimetry data from the satellite missions CryoSat-2 (CS-2) and Sentinel-3 (S-3) A & B. The most recent Baseline 005 of the Sentinel-3 Sea Ice Thematic Product with the "Land" Processing Segment includes Sentinel-3 L1B pre-processed with the same configuration as CryoSat-2 (Aublanc et al., 2025), so we used observations from the three sensors interchangeably. CS-2 carries a SAR Interferometric Radar Altimeter (SIRAL) operating at a Ku-band central frequency of 13.575 GHz. Over sea ice the device mainly operates in SAR mode. The Doppler processing in SAR mode results in higher along-track resolution of ∼350 m when compared to the conventional pulse-width limited altimetry, resulting in a footprint size of ∼350x1600 m and coverage extends up to 88°North (ESA, 2026). The Sentinel-3A and -3B missions carry the SAR Radar ALtimeter (SRAL) sensor which operates at dual Ku/C-band frequency (13.575/ 5.41 GHz). The SAR processing at Ku-band produces a similar footprint size as CS-2 (Aublanc et al., 2025). The S-3 satellites only provide coverage up to 81.5°North, which is a benefit to this study because the Øer Ice Barrier lies around 80°N and is therefore well-covered near the orbital limit of S-3. Here, we used waveforms from the CS-2 level 2 baseline E SAR-mode product and S-3 level 2 baseline 005 product.

3.3 In situ measurements

The *CIRFA-22* research cruise onboard RV *Kronprins Haakon* visited the Øer Ice Barrier in April–May 2022, providing a unique data set of snow and sea ice measurements in late Winter conditions. Snow and ice measurements were taken at three different locations on the fast ice, covering both level FYI and MYI, as shown in Fig. 1. The sampling locations were inside or in close vicinity of the outlined ROIs and hence the in situ data is considered representative for the FYI and MYI in the ROIs. All measurements were obtained between 27 April and 3 May 2022, when air temperatures were in the range -20 to -7°C. In the context of this study we used the following measurements: ice thickness from drill holes, snow properties from pits, snow and sea ice thickness data from collocated transects with a Magnaprobe (Sturm and Holmgren) and surface-

https://doi.org/10.5194/egusphere-2026-1662
Preprint. Discussion started: 26 March 2026

based electromagnetic sounding (GEM-2 by Geophex Ltd., hereafter referred to as GEM) instrument, and vertical temperature profiles at 2 cm resolution in the snow and ice over the course of several weeks obtained from a Snow and Ice Mass Balance Apparatus (SIMBA) (Thompson et al., 2025).

A total of 10 snow pits were dug, spread over the three different ice stations and covering both FYI and MYI. The following physical snow properties were characterized layer-wise: density, grain size and type, and hardness. Temperature and salinity were measured at vertical resolutions of 5 and 3 cm, respectively. At every snow pit and at a few additional locations a bulk snow water equivalent (SWE) measurement was taken too. Ice cores were drilled at all three ice stations too and provide ice temperature, salinity, and density measurements. The latter were obtained through hydrostatic weighing. One collocated GEM and Magnaprobe transect is available over FYI, and another one over MYI. The SIMBA was deployed on MYI at the southern ice station and collected data from 28 April to 29 May 2022. The instrument recorded a vertical temperature profile every 6 hours (including air temperatures just above the snow surface) and a heat conduction cycle every 24 hours, from which snow depth and ice thickness was estimated. The reader is referred to the *CIRFA-22* cruise report (Dierking et al., 2022) for detailed information about the in situ measurements.

The in situ data are inherently limited in quantity and spatial coverage, only available for a short time span. These data are nonetheless valuable for a quantitative assessment of the satellite retrievals, as they are independent samples that are not susceptible to the same error sources and biases as the remote sensing observations. Furthermore, knowledge of in situ snow and ice properties helps to better constrain some of the free parameters in the satellite retrievals, such as snow and ice density in altimetry-derived ice thickness estimation.

3.4 Meteorological data

The SIMBA instrument provided in situ measurements of air temperature for the month of May only. We therefore also retrieved in situ daily averages of 2-m air temperature from the meteorological station Henrik Krøyer Holme (HKH) between 15th January and 5th August 2022. This station is located on an island near the Greenland coast, roughly 150 km north-west of our study sites and is operated by the Danish Meteorological Institute (DMI). The data was retrieved through the DMI Climate Data API (last accessed on 21 July 2025). In addition, air temperatures and daily total precipitation were retrieved from reanalysis over the same time period, providing estimates at larger scales and over the exact area of the study. We retrieved 2 m air temperatures at 12-hourly intervals and daily total precipitation over the Øer Ice Barrier from the Copernicus Arctic Regional ReAnalysis (CARRA) model (Schyberg et al., 2020), which comes at a 2.5 km horizontal resolution. Air temperatures from the HKH weather station were likely assimilated in CARRA. We determined the phase of the precipitation (rain or snow) at 3-hourly intervals using a linear approximation of the suit of exponential curves formulated in (Dai, 2008), with a center fraction of 0.5 at 1.1°C.

The time series of air temperatures and precipitation is visualized in Fig. 2. As can be seen in this figure, the air temperatures of the different sources are in good agreement with each other. Spearman's correlation between CARRA and HKH 2m air temperatures for the entire time of the study is 0.93 and the RMSE is 3.1°C. The SIMBA air temperatures correlate more with air temperatures from CARRA than from HKH, with a correlation of 0.93 compared to 0.75, and RMSE of 1.6 versus 3.2 °C.

https://doi.org/10.5194/egusphere-2026-1662
Preprint. Discussion started: 26 March 2026

The air temperatures modeled by CARRA thus seem to provide better estimates of local conditions over the study site, at least during the month of May, and we therefore used the CARRA air temperatures as reference in the remainder of this study. The figure also shows that before 1 June there are only three occasions where (part of the) precipitation fell as rain.

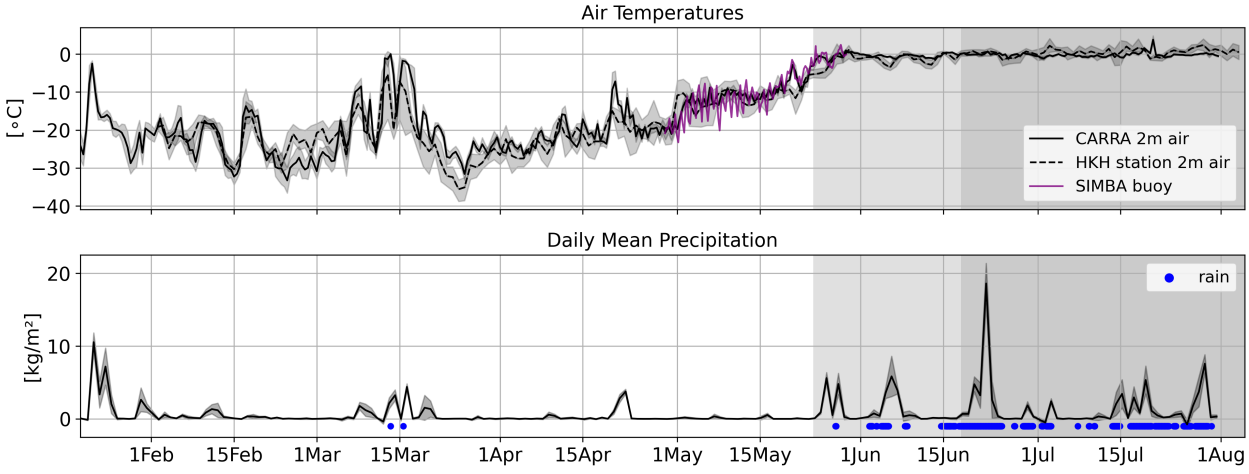

Figure 2.

Air temperature and daily mean precipitation over the Øer Ice Barrier in Spring 2022. Air temperatures are shown for different data sources: CARRA reanalysis, Henrik Krøyer Holme (HKH) weather station, and SIMBA. Precipitation is only available from reanalysis (CARRA).

4 Methods

4.1 Definition of seasons

The time series covers both freezing and melting conditions. During the freezing conditions, a warming event occurred in mid-March with temperatures approaching zero degrees and strong snowfall lasting for ∼1 week. The transition period from freezing to melting conditions takes place in May–June. For this study, we defined three seasons relevant from a remote sensing perspective, based on definitions that have been used in previous studies (Yackel et al., 2001; Karlsen et al., 2024): Winter, melt onset, and advanced melt. The start of melt onset was defined as the first occurrence of a positive temperature in either the HKH station data, the CARRA reanalysis data, or the SIMBA data. Similarly, the transition from melt onset to advanced melt was defined as the latest date when temperatures are above zero degrees for at least 48 hours consecutively in all three data sources. Using these definitions, melt onset starts on 24 May and advanced melt on 16 June 2022 (see Fig. 2). We provide a visual reference of these seasons in all time series plots by coloring the melt onset period in light gray and advanced melt in dark gray.

https://doi.org/10.5194/egusphere-2026-1662
Preprint. Discussion started: 26 March 2026

4.2 In situ measurements

The non-autonomous in situ measurements were taken between 27 April–3 May, which is in late winter but well before melt onset. The SIMBA instrument recorded data until 29 May, hence covering the transition from late winter to melt onset. We used the in situ measurements to obtain an average snow and ice density value per ice type, as well as distributions of snow and ice thickness per ice type. The average snow density was obtained by averaging the bulk SWE measurements per ice type. The bulk SWE values are preferred over averaging layer-wise densities from snow pits, since ice lenses and crusts in the snowpack are hard to sample with a density cutter and can therefore lead to underestimation of the snow density. Regarding ice density, one average value was calculated per ice type based on density measurements from ice cores obtained by hydrostatic weighing. In situ snow and ice thickness distributions were inferred from the collocated GEM and Magnaprobe transects. Total snow plus ice thickness values were extracted from the GEM in-phase component at 18330 Hz, following the approach described in (Itkin et al., 2023). The GEM device has a higher sampling frequency than the Magnaprobe, which has an irregular sampling frequency due to the manual handling. The Magnaprobe data was upsampled to the GEM sampling frequency by finding the spatially closest Magnaprobe sample for each GEM data point via a nearest neighbor search.

4.3 SAR

Pre-processing of the S-1 images included denoising, radiometric calibration to σ_0, multi-looking the image with a window size of 3×3, conversion to decibels, and geocoding to polar stereographic projection (EPSG 3996) at a pixel spacing of 100 m. When investigating the radar backscatter evolution in a SAR time series that is not made up of repeat pass images, it is important to correct the backscatter values for variations in incidence angle (Yackel and Barber, 2000; Geldsetzer and Howell, 2023). This process is referred to as *incidence angle normalization* and implies finding a slope estimate and subsequently mapping all backscatter values to a common incidence angle using this slope estimate. Here, we estimated a slope from the SAR time series during the winter period using the differencing method presented in (Geldsetzer and Howell, 2023), where a slope estimate is calculated for each successive pair of SAR images where the same ice is imaged at two different incidence angles. The average slope value per ice type was then used to project the backscatter values onto a common incidence angle of 35°for the entire SAR time series, including the melt season. See Appendix A1 for a detailed description of the incidence angle normalization procedure and slopes used here.

4.4 Radar Altimetry

4.4.1 Retracking

We re-tracked the CS-2 and S-3 waveforms using the Lognormal Altimeter Retracker Model (LARM), a physical-model retracker with a variable percentage threshold determined by the large-scale surface roughness and backscattering efficiency of the sea ice (Landy et al., 2020). Compared to retrackers with a fixed threshold, the variable threshold method can theoretically resolve thinner freeboards - down to a few centimeters - even over newly-formed ice with a very smooth surface, as well as

https://doi.org/10.5194/egusphere-2026-1662
Preprint. Discussion started: 26 March 2026

thicker and rougher freeboards (Landy et al., 2020). Monitoring sea ice growth from its initial formation stage enables us to test the capability of the retracker to profile thinner and smoother ice, and to ascertain any systematic bias in altimetry freeboard when ice thickness should be close to zero.

4.4.2 Waveform parameters

Different thresholds on varying waveform parameters exist to distinguish between echo returns from *leads* and *sea ice*, depending on the re-tracker algorithm used (Ricker et al., 2014). In this context, we retrieved the time series of the following commonly-used radar waveform parameters per ice type: sigma nought radar backscatter coefficients (σ_0), leading edge width (LEW) calculated for power thresholds of 5 and 95%, and pulse peakiness (PP) as formulated in (Ricker et al., 2014). The LEW mainly characterizes the influence of surface topography on the fitted waveform, while the PP is a measure of the specularity of the waveform (Wingham et al., 2006; Laxon, 1994). These waveform parameters are strongly correlated.

The σ_0 backscatter coefficients obtained with the S-3 sea ice retracker have not been calibrated against backscatter from CS-2 and therefore a significant offset in backscatter is observed between both sensors. We quantified the horizontal offset between the backscatter distributions from both sensors using the 1-D Wasserstein distance (Panaretos and Zemel, 2019) and found the offset to be 21 dB. We then align the S-3 backscatter values to the CS-2 ones by subtracting 21 dB from the S-3 backscatter coefficients. See Appendix A3 for more details.

4.4.3 Removing false lead tiepoints

Visual comparison of spatio-temporally overlapping SAR and along-track radar freeboards revealed that many radar waveform returns over the FYI ROIs in both CS-2 and S-3 were wrongly classified as leads, even weeks after the ice had initially formed. Over the newly-formed FYI areas, median LEW values are ∼0.5, PP in the range 50–100, and σ_0 backscatter in the range 20–30 dB. Typical thresholds for classifying a waveform as *lead* are LEW<=0.75, PP>=66, and σ_0>23 dB (Cryo-TEMPO and AWI products). The returns over newly-formed, smooth FYI often meet all three requirements and hence get misclassified.

These wrongly classified returns bias surrounding freeboard estimates low. Here, we wished to focus on the impact of snow and sea ice radar scattering biases on retrieved freeboards. So, as this issue appeared to be quite persistent in many of the ROIs in the time period after ice formation (with a few misclassifications even up to April), we excluded all lead tie points within the fast ice between February–April, and re-processed the CS-2 and S-3 freeboards using only lead tie points identified in the drift ice. This was achieved by applying a fast-ice mask (see Fig. 1) before identifying lead tie points to calculate freeboard values. See Appendix A2 for a detailed description of the method used here.

4.5 Laser Altimetry

4.5.1 Custom interpolation scheme for freeboard derivation in lead-sparse areas

The IceSat-2 ATL10 freeboard product as provided by NSIDC does not contain freeboard values for samples where the closest lead tie point is more than 10 kilometeres away (Kwok et al., 2023). Since the ROIs in this study are located in an area of

https://doi.org/10.5194/egusphere-2026-1662
Preprint. Discussion started: 26 March 2026

immobile landfast ice, this distance restriction was often problematic and the lack of sea surface height samples led to scarce ATL10 freeboard data over the ROIs - even in locations where a valid ATL07 surface height had been obtained. Adding to this problem is the fact that lead tie points cannot be used across the six IS-2 beams when calculating sea surface height anomaly (SSHA) estimates, because the different beams have not yet been calibrated against each other and centimeter-scale deviations in range remain (Bagnardi et al., 2021). To improve the laser altimetry coverage, we implemented a custom freeboard derivation where the closest lead tie point can be up to 100 kilometers away. For each ATL07 surface height sample the ten closest lead tie points along the same beam were identified with a k-nearest neighbor search. An interpolated SSHA was then calculated for each ATL07 sample where no ATL10 freeboard was available, using an inverse distance squared weighted interpolation of the SSHA of the 10 nearest neighbours, as given by Eq. (1).

$$\text{SSHA}[i]_{interpolated} = \frac{\sum_{k=1}^{10} \left(\text{SSHA}_k \cdot \frac{1}{D_k^2} \right)}{\sum_k \frac{1}{D_k^2}} \tag{1}$$

Here k is the k-th nearest lead tie point of sample i in the ATL07 heights and D the distance from this sample to the lead tie point. The freeboard value then equals the ATL07 height minus the interpolated SSHA, as given by Eq. (2). Samples that have an original ATL10 freeboard value are kept as such.

$$\text{FB}[i] = \begin{cases} \text{h}[i]_{ATL07} - \text{SSHA}[i]_{interpolated} & \text{if FB[i]}_{ATL10} = NaN \\ \text{FB}[i]_{ATL10} & \text{otherwise} \end{cases} \tag{2}$$

We re-processed all IS-2 freeboards in this manner to obtain better laser altimetry coverage over the ROIs. We validated the new freeboard values by comparing all sets of beams from tracks intersecting within radii of 250, 500, and 1000 m over the fast ice within a time interval of at most 10 days ($\simeq$ 240 hours). Figure 3 shows the laser freeboards for pairs of intersecting beams within a radius of 1000 m, colour-coded by time lag and with the corresponding Spearman correlation coefficient (R). On the sides of the scatterplot, kernel density estimates obtained using a Gaussian kernel are shown per time lag. The plot shows that laser freeboard retrievals generally exhibit a high correlation between two overpasses. Some variability is expected due to the nature of the experiment, as we do not look at exact repeat passes, but rather at intersections where track A does not sample the exact same ice surface as track B. The correlation coefficients range between 0.67–0.87. Based on these results, we concluded that the interpolation scheme for increased IS-2 coverage provides reliable freeboards and hence these new data points were included into the study. Appendix A4 provides more details about the intersection analysis.

https://doi.org/10.5194/egusphere-2026-1662
Preprint. Discussion started: 26 March 2026

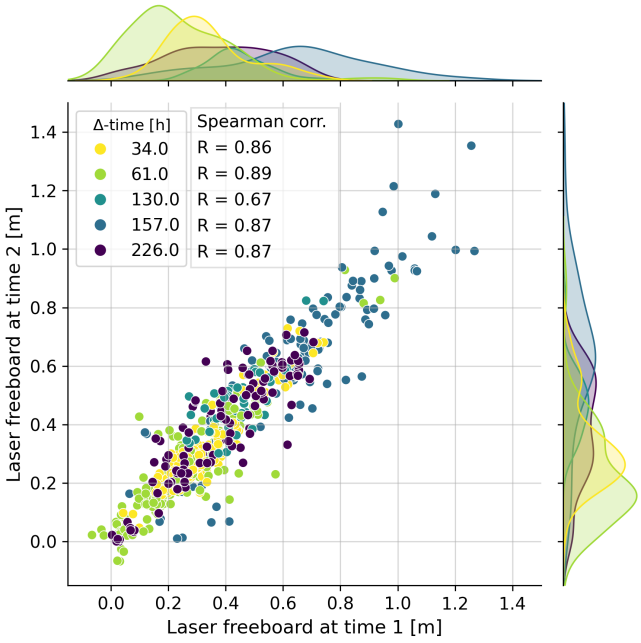

Figure 3. Comparison of laser freeboards for pairs of intersecting IS-2 beams, colour-coded by time lag. Spearman's correlation coefficient (R) is reported per time lag and kernel density estimated PDF's are shown on the sides.

4.6 Laser and radar freeboard time series construction

This section describes how data from the individual ROIs were combined to obtain one laser freeboard and one radar freeboard time series per ice type.

The ice surface within ROIs of the same ice type had a fairly similar radar signature in the SAR images. Moreover, all FYI regions formed within a span of four weeks and matured similarly since the ice was immobile and therefore only grew thermodynamically. The different ROIs of one ice type could thus be considered as subsets sampling the same ice, i.e. be considered as one large ROI. This implies that the along-track freeboards from an altimetry track crossing any of the ROIs is a representative sample for the corresponding ice type. With this reasoning in mind, all altimetry tracks from IS-2, CS-2, and S-3 that intersected with any of the ROIs in the time frame of the study were gathered per ice type, with the benefit of finer temporal sampling of the time series. For each intersection we calculated the median and inter-quartile range (IQR) of the along-track freeboards that are within the ROI boundaries. This spatial averaging is desired as along-track radar freeboards from CS-2/S-3 contain random errors due to speckle noise and uncertainties in sea surface height interpolation (Wingham et al., 2006; Ricker et al., 2014). Using the median instead of mean prevents outliers from influencing the results. The result is a timestamp and corresponding median freeboard plus IQR that feeds into the time series. We used laser freeboards from the six IS-2 beams

https://doi.org/10.5194/egusphere-2026-1662
Preprint. Discussion started: 26 March 2026

and considered them as equivalent, as freeboard is a relative measure and therefore inter-beam biases in absolute range cancel out. The result is a time series of laser and radar freeboards per ice type.

For FYI the time series was constructed in a relative way too, meaning that timestamp t=0 is the ice formation date. This was achieved by referencing every freeboard sample to the formation date of the ROI this sample originates from. The result is a relative time series that visualizes the seasonal evolution of FYI, which includes the initial ice formation, snow accumulation and ice growth, and subsequent melt. The relative time series captures the evolution of altimetry signatures from newly-formed ice to snow-covered FYI more accurately by accounting for the differences in ice evolution between ROIs in the first few weeks after ice formation. The drawback with the relative approach is that it is not possible to directly link the time series to atmospheric events on specific dates. We set 8 February as t=0 in the plots for the relative FYI time series, which corresponds to the average FYI ice formation date. The MYI time series was only constructed in absolute time, as here the ice was already matured and snow-covered when we started monitoring it and hence no significant changes were expected at short time scales. The MYI time series is meant to serve as a reference in the interpretation of the FYI time series.

The time series of radar freeboards are more dense than the laser ones, as there are three radar altimeters and only one laser altimeter. This effect is amplified by S-3A&B having a much higher temporal resolution and spatial coverage over the Øer Ice Barrier compared to CS-2 and IS-2. A regular sampling grid was needed to calculate dual-frequency snow depth, so we interpolated the laser and radar freeboard time series at daily resolution using a Radial Basis Function interpolator with a Gaussian kernel with standard deviation of 11.8. The temporal smoothing further mitigated the random errors that affect the median radar freeboards derived from individual altimeter crossings and helped to reveal actual trends in the time series.

4.7 Freeboard-to-thickness conversion

Under the assumption of isostatic equilibrium, ice freeboard (FB_i) can be converted to ice thickness (SIT) using Eq. (3), provided that the snow depth (SD) and densities of snow (ρ_s), sea ice (ρ_i), and sea water (ρ_w) are known (Laxon et al., 2003). This section outlines how we determined values for snow and ice densities, and how we estimated snow depth.

$$SIT(FB_i, SD) = \frac{\rho_w}{\rho_w - \rho_i} FB_i + \frac{\rho_s}{\rho_w - \rho_i} SD \tag{3}$$

4.7.1 Density of snow, sea ice, and sea water

Snow – Choosing an appropriate bulk snow density is challenging because the density of snow can be highly variable at short spatiotemporal scales - both in the vertical and horizontal direction. We based the snow densities for this study on in situ values from 10 snow pits dug in late April during the *CIRFA-22* cruise. Snow on sea ice tends to densify throughout the season (Barber et al., 1995). We therefore implemented a linear time-dependent equation for snow density, using the seasonal densification rate identified in (Mallett, 2025) and calibrated the offset to match the in situ snow density measurements of late April, which were: 298 +/- 81 kg/m^3 for FYI and 302 +/- 66 kg/m^3 for MYI. This results in Eq. (4) for FYI and Eq. (5) for MYI, where T_a is the number of days since ice formation for FYI, and the number of days since 1 August for MYI. For FYI we calculated T_a

https://doi.org/10.5194/egusphere-2026-1662
Preprint. Discussion started: 26 March 2026

relative to the average ice formation date of all FYI ROIs, which was 8 February 2022. This was deemed reasonable since all FYI ROIs formed within two weeks from this date.

$$\rho_{FYI} = 0.35T_a + 270 \tag{4}$$

$$\rho_{MYI} = 0.35T_a + 207 \tag{5}$$

Sea ice – For ice density (ρ_i), common approaches include an ice type-dependent definition of density based on field measurements from the 1980's, or using a single ice density (Kacimi and Kwok, 2024). The single value approach might arguably better represent the ice density in the current Arctic, as more recent studies indicate that MYI densities appear to be closer to the FYI ones, especially for younger MYI (Jutila et al., 2022). Commonly used values are 917 kg/m^3 for FYI and 882 kg/m^3 for MYI, or 915–917 kg/m^3 when using a single value (Kacimi and Kwok, 2024). In reality, ice density varies throughout the season and additionally depends on ice type, age, temperature, and thickness (Salganik et al., 2025). Jutila et al. (2022) found a negative exponential relationship between Arctic spring sea ice freeboard and density. However, at present there is no conclusive parametrization for the temporal evolution of sea ice density over the course of a winter season. We therefore considered the in situ ice density values obtained from the ice cores at the end of April as the best estimates of ice density in our ROIs and used these values for the entire time series. The average value for FYI obtained from the cores was 914 +/- 2 kg/m^3, while for MYI it was 909 +/- 3 kg/m^3.

Sea water – For near-surface sea water (ρ_w) we used the conventional density of 1024 kg/m^3 (Wadhams et al., 1992).

4.7.2 Snow depth from laser and Ku-band radar freeboards ("LaKu")

Snow depth estimates can be obtained from near-coincident laser and radar freeboard observations (Kwok et al., 2020; Fredensborg Hansen et al., 2024; Carret et al., 2025). Dual-altimetry snow depth is derived by differencing the laser freeboard (FB_{La}) from the ice freeboard (FB_i):

$$H_s = FB_{La} - FB_i \tag{6}$$

The ice freeboard can be obtained from the radar freeboard (FB_{Ku}) by accounting for the slower propagation speed of radar waves in snow (c_s) compared to free space (c) (Ulaby et al., 1981). The refractive index for snow (n_s) is dependent on the snow density (ρ_s) as given by Eq. (7) (Ulaby et al., 1981) and is used to convert FB_{Ku} to FB_i using Eq. (8).

$$n_s = \frac{c}{c_s} = (1 + 0.00051\rho_s)^{1.5} \tag{7}$$

$$FB_i = FB_{Ku} + SD\,(n_s - 1) \tag{8}$$

https://doi.org/10.5194/egusphere-2026-1662
Preprint. Discussion started: 26 March 2026

By substituting Eq. (8) into (6) and solving for SD, the following expression for snow depth is obtained:

$$SD = \frac{FB_{La} - FB_{Ku}}{n_s} \tag{9}$$

Note that this expression is dependent on snow density through the refractive index n_s. Equation 9 was used to calculate a daily SD estimate from the interpolated laser and radar freeboard time series, using the time-dependent snow densities as defined in Eq. (4) and (5) for FYI and MYI, respectively.

4.7.3 Ice thickness from radar freeboard

The freeboard-to-thickness conversion outlined in Eq. (3) requires FB_i as input. Radar freeboards are linked to ice freeboards via Eq. (8), so by plugging Eq. (8) into (3), an expression for ice thickness as function of radar freeboard is obtained:

$$H_i(FB_{Ku}, SD) = \frac{\rho_w}{\rho_w - \rho_i} FB_{Ku} + \frac{\rho_w \left(1 + 00051\rho_s\right)^{1.5} - \rho_w + \rho_s}{\rho_w - \rho_i} SD \tag{10}$$

The dual-altimetry snow depths and densities outlined above were used in this equation to convert the radar freeboard time series into an ice thickness time series per ice type.

4.8 Modeled ice growth

To provide context for the snow depth and ice thickness time series obtained from the altimetry observations and support its interpretation, we modeled snow accumulation and thermodynamic ice growth at the FYI and MYI sites during the period of the study. Since the ice was immobile, we can assume the ice did not thicken dynamically through ridging, so that total ice growth was exclusively thermodynamic. We used a combination of SnowModel and HIGHTSI as decribed in Itkin and Liston (2025). The model was initialized by 0.3 m sea ice thickness on 10 October 2021 for MYI and by zero ice thickness on 8 February 2022 for FYI, which corresponds to the average formation date of the FYI regions. Afterwards, the model was forced with the air temperature and precipitation data from CARRA (see Sect. 3.4). The surface ocean heat fluxes and other variables do not have a significant impact on the simulation results and were set as in Itkin and Liston (2025). The snow depths and densities from in situ observations (Sect. 3.3) were assimilated to correct the bias in precipitation, and the sea ice thickness was simulated based on these adjusted snow properties. The main focus is the modeled ice growth and snow accumulation of FYI, since this is well-constrained and as such provides a good reference for the altimetry-derived SIT and LaKu snow depth.

4.9 Modeled dielectric properties of snow on sea ice

4.9.1 Complex dielectric constant of snow

The presence of salt in snow impacts radar wave propagation because it introduces liquid water in the snow at temperatures below 0°C. The liquid water alters the complex dielectric constant of the snow, leading to increased absorption (Ulaby et al.,

https://doi.org/10.5194/egusphere-2026-1662
Preprint. Discussion started: 26 March 2026

1981; Barber and Fung, 1998; Geldsetzer et al., 2009). Here, we investigated the impact of saline snow on Ku-band wave propagation by modeling the complex dielectric constant in fresh (i.e. MYI) versus saline (i.e. FYI) snow at Ku-band frequency. The salt content is typically highest at the base of the snow pack, so we modeled the complex dielectric for the basal layer only as this will highlight the differences between saline and fresh snow. The complex dielectric constant of the snow (ε_s) was estimated using the frequency dispersion model of (Geldsetzer et al., 2009) as formulated in Eq. (11), which allows for either fresh or saline snow.

$$\varepsilon_s = \varepsilon'_s - i\varepsilon''_s \quad where \quad \varepsilon'_s = \varepsilon'_{ds} + S\varphi\varepsilon'_b \quad and \quad \varepsilon''_s = \varepsilon''_{ds} + S\varphi\varepsilon''_{b(\mathrm{rel})} + \varepsilon''_{s(\mathrm{cond})} \tag{11}$$

With ε_s, ε_{ds}, and ε_b the complex dielectric constants of snow, dry snow and brine, respectively, S the depolarization factor, φ the brine volume fraction. The contributions from relaxation (rel) and conductivity (cond) to ε''_b are treated separately (Geldsetzer et al., 2009). Estimating the input parameters requires knowledge about the snow temperature, density, salinity, and crystal size. Here, we quantified these variables from the in situ data. We used snow temperatures measured by the SIMBA instrument in the snow layer 0–4 cm above the snow/ice interface, available from late April until the end of May. This covered the time period leading up to melt onset, where temperatures gradually rose from ∼-20 to 0°C. For the snow properties, we used the median salinity, density, and crystal size from the bottom 10% of the snow pits, per ice type. These snow properties were observed in late April and were used here to model the snow throughout the month of May due to the lack of repeat measurements. We expect, however, that the first-order mechanisms responsible for changes in the dielectric snow properties at microwave frequencies are still modeled correctly through the coupled temperature-salinity effects, assuming that the snow did not significantly desalinate over the course of these four weeks.

4.9.2 Radar penetration depth

Changes in the dielectric properties of the snow impact the characteristic distance an electromagnetic wave can penetrate into the snow layer. The penetration depth is defined as the depth into a medium at which the power of the wave is reduced to a factor e^{-1} the power of the incident wave at the upper surface of the medium (Ulaby et al., 1981). We modeled the radar penetration depth into the basal snow layer, i.e. the bottom 10% of the snow pack, at Ku-band frequency for the time period in situ snow temperatures are available from the SIMBA instrument. The modeled penetration depth gives a theoretical lower bound on the depth inside the basal snow layer from where significant radar energy is expected to return to the sensor, assuming an idealized snow layer where surface scattering at the air/snow interface is minimal. Note that this single-layer model does not take into account the presence of ice underneath the snow and hence does not include surface scattering at the snow/ice interface. The goal here was to model how the presence or absence of salt in the basal snow layer affects the Ku-band radar penetration depth inside this snow layer. The radar penetration depth (δ_p) was modeled as:

$$\delta_p = \frac{\lambda}{4\pi}\left\{\left[\left(1+\left(\frac{\varepsilon''}{\varepsilon'}\right)^2\right)^{1/2} - 1\right]\frac{\varepsilon'}{2}\right\}^{-1/2} \cdot cos(\theta_i) \tag{12}$$

https://doi.org/10.5194/egusphere-2026-1662
Preprint. Discussion started: 26 March 2026

where λ is the wavelength, ε' and ε'' are real and imaginary part of the complex dielectric constant of the basal snow layer, and $cos(\theta_i)$ the incidence angle of the EM-wave (Ulaby et al., 1981). The complex dielectric constant of the snow was estimated through Eq. (11), for saline (FYI) and fresh (MYI) snow. For nadir-looking sensors, such as the radar altimeters CS-2 and S-3, the incidence angle was set to zero.

5 Results

5.1 In situ snow and ice properties

Ten snow pits were physically sampled in the study area between 27 April–3 May 2022, seven on FYI and three on MYI (see Fig. 1 for locations). All studied snow packs showed typical characteristics of snow on Arctic sea ice in late Winter. Every snow pit was characterized by a soft, low-density basal layer composed predominantly of depth hoar crystals with diameters in the range 0.5–6 mm (FYI) and 0.5–11 mm (MYI). For all FYI pits this bottom layer was saline, with salinity values between 3–6 PSU and a mean of 4.2 PSU. Saline snow was found up to 6 cm away from the snow/ice interface, albeit at lower salinity values higher up in the snow pack (salinity $<$1 PSU at 6 cm). The upper layers of the pits were more varied, but generally had a higher density and smaller crystals, often faceted or rounded, which is characteristic for Arctic snow packs (Sturm et al., 1827). Some pits had ice lenses and crusts that were potentially formed during the warming event in March. Figure 4 shows the median snow temperature, salinity, and hardness in 10% height intervals. The average snow density obtained from bulk SWE measurements was: 298 +/- 81 kg/m^3 for FYI and 302 +/- 66 kg/m^3 for MYI. Regarding ice density, the average value for FYI obtained from the cores was 914 +/- 2 kg/m^3, while for MYI it was 909 +/- 3 kg/m^3.

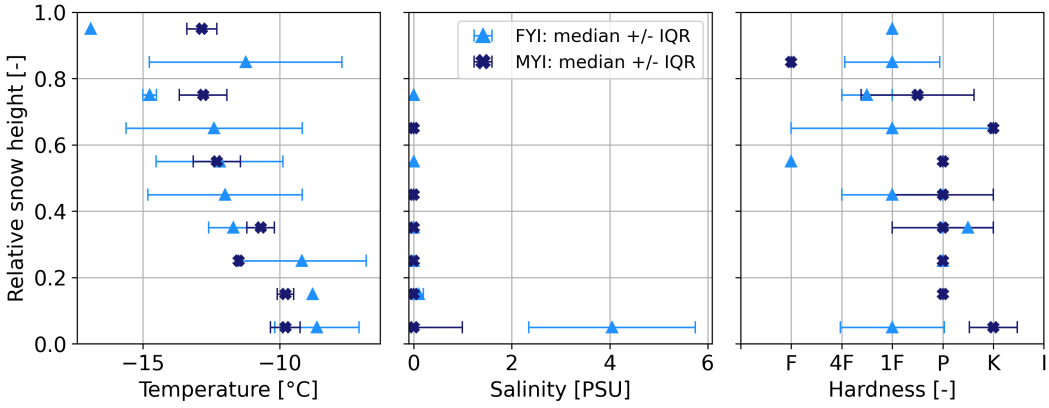

Figure 4.
in situ snow properties per 10% height intervals: temperature, salinity, and hardness. The hardness letter codes are: fist (F), 4 fingers (4F), 1 finger (1F), pencil (P), knife (K), ice (I) (Fierz et al., 2009). Profiles are shown in relative snow height, with 0 the bottom and 1 the top of the snow pit.

https://doi.org/10.5194/egusphere-2026-1662
Preprint. Discussion started: 26 March 2026

Snow depth and ice thickness distributions from collocated GEM and Magnaprobe transects are visualized in Fig. 5. Over FYI the ice was 0.92 ± 0.15m with a snow cover of 0.18 ± 0.15m, while over MYI the ice was 2.03 ± 0.52m with 0.34 ± 0.17m snow.

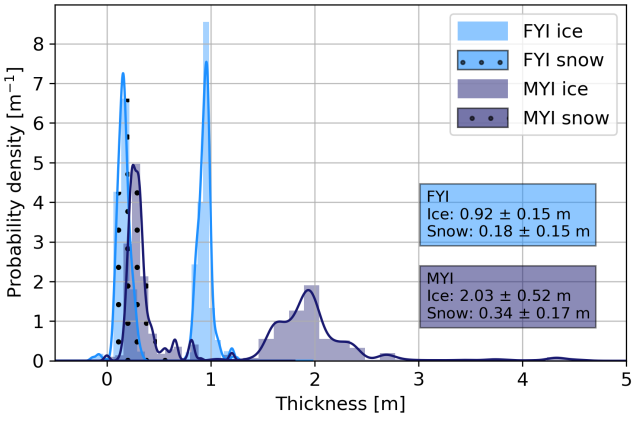

Figure 5.
Ice and snow thickness distributions from collocated GEM and Magnaprobe transects over FYI and MYI in the Øer Ice Barrier at the end of April.

5.2 Temporal evolution of laser and radar freeboards

Panels a), b), and c) in Fig. 6 show the time series of radar and laser freeboards for FYI (relative and absolute time) and MYI, respectively. The original data points are shown as light-colored markers with error bars (median+IQR) and the daily interpolated values in darker color. Black vertical lines indicate the timestamps at which we start tracking different individual ROIs. Note it is the radar freeboards that are shown here, so no correction for slower wave propagation in snow is applied.

For FYI, the moment of ice formation is best captured in the relative time series (panel (a)), while changes due to atmospheric conditions, such as the warming event or melt onset, are best analyzed from the absolute time series (panel (b)). The moment of ice formation is marked by relatively high radar freeboards (∼ 0.07 m), while laser freeboards are lower(∼0.04 m) but still largely above zero. Within a week after ice formation the laser freeboards start rising, while radar freeboards initially drop to values just below zero and only start rising approximately 2 weeks after ice formation. In both the relative and absolute time series, the laser freeboards rise at an average rate of 0.25 cm day^{-1}, representing snow accumulation and sea ice growth, until reaching a maximum around 0.22 m in the middle of May. Radar freeboards show a slight positive trend of 0.06 cm day^{-1} in the same time period. Laser freeboards tend to increase stepwise, following the precipitation events, while the radar freeboards show a more linear increase throughout the winter period. Note that the sudden jumps in laser freeboards following precipitation events are smoothed out in the interpolated time series and appear less pronounced. The absolute time series shows that radar freeboards exhibit a temporary rise of ∼5 cm around 15 March, coinciding with the warming event. An opposite dynamic is

https://doi.org/10.5194/egusphere-2026-1662
Preprint. Discussion started: 26 March 2026

observed around 10 May, when radar freeboards temporarily drop. There is no laser coverage in the second half of May, so the exact time when laser freeboards start decreasing is unknown. The rate of decrease in the second half of May is 0.7 cm day^{-1}, but is likely underestimated due to the data sparsity. After this steep decline, laser freeboards stabilize ∼0.5 m later in the melt onset period. Radar freeboards, however, continue increasing well into melt onset, at an accelerated rate of 0.63 cm day^{-1} until reaching a peak of ∼0.08 m on 8 June - nearly one month after the laser freeboards reached their maximal value. Between 17 May and 8 June multiple individual crossings have a median radar freeboard in the range 0.1–0.2 m, while the bulk of all freeboards measured throughout the winter period lie in the range -0.1–0.1 m. In late melt onset the radar freeboards drop at a rate of 0.4 cm day^{-1} towards small negative values in advanced melt. Apart from the first days after ice formation and the peak at melt onset, median radar freeboards consistently remain below median laser freeboards.

The MYI regions have already accumulated snow over the course of several months before we start tracking them in February. This is reflected in laser freeboards that are consistently 0.3–0.4 m higher than the radar freeboards during the winter period. Laser freeboards initially drop from ∼0.6 m to ∼0.4 m, before rising and stabilizing ∼0.6 m from 1 April until melt onset. Radar freeboards start in the range 0.1–0.2 m and increase with a trend of 0.24 cm day^{-1} until approximately 15 March, when values stabilize ∼0.2–0.3 m for the remainder of winter. At melt onset, freeboards gradually start decreasing for both sensors. The rate of decrease is higher for radar freeboards (-0.93 cm day^{-1}) than for laser freeboards (-0.56 cm day^{-1}), although it must be noted that only two IS-2 crossings are available in the melt onset time period. The radar freeboards stabilize at values close to zero by the start of advanced melt, while the laser freeboards continue decreasing for another 20 days in advanced melt.

In Fig. 7 and 8 the evolutions of the laser and radar freeboards are visualized as distributions per 15-day time intervals for FYI and MYI, respectively. Radar freeboard distributions are drawn separately for CS-2 and S-3 to examine the consistency of freeboards obtained from these different sensors. For FYI the distributions neatly capture the cycle of a seasonal ice cover: initial ice formation (day 0–15), followed by a period of ice growth and rapid snow accumulation (day 15–60), slowed ice growth and snow accumulation (day 60–105), and eventually melt (day 105–150). In the stage of initial ice formation (day 0–15) the laser and radar distributions are peaky, with lowest IQRs, and overlap with a median freeboard close to zero. It is notable that the laser freeboards thicken rapidly and are separated from the laser freeboards after only ∼2 weeks. In the period of ice growth and snow accumulation (day 15–105), the laser freeboards increasingly shift towards higher values, while the radar freeboards first remain relatively constant and low and only show a slight increase towards the end of the winter period. For both frequencies the inter-quartile range (IQR) increases though. During early melt onset (day 105–120) we observe a drop in laser freeboards and a narrower distribution, while the radar freeboards show an increase in median value and even more so in variance. Later during melt onset (day 120–135), a bimodal distribution is observed for the laser freeboards. However, some of the variability in the shape of the laser distributions could be due to the limited amount of samples available in a 15-day time period. In advanced melt, both the laser and radar freeboards continue decreasing towards zero.

The freeboard distributions over MYI (Fig. 8) clearly reflect the different seasons. Note the scale difference on the x-axis compared to the FYI distributions. The winter period shows a relatively stable situation with median laser freeboards well above the radar freeboards. The distributions have a much higher IQR compared to FYI, especially for the laser observations.

https://doi.org/10.5194/egusphere-2026-1662
Preprint. Discussion started: 26 March 2026

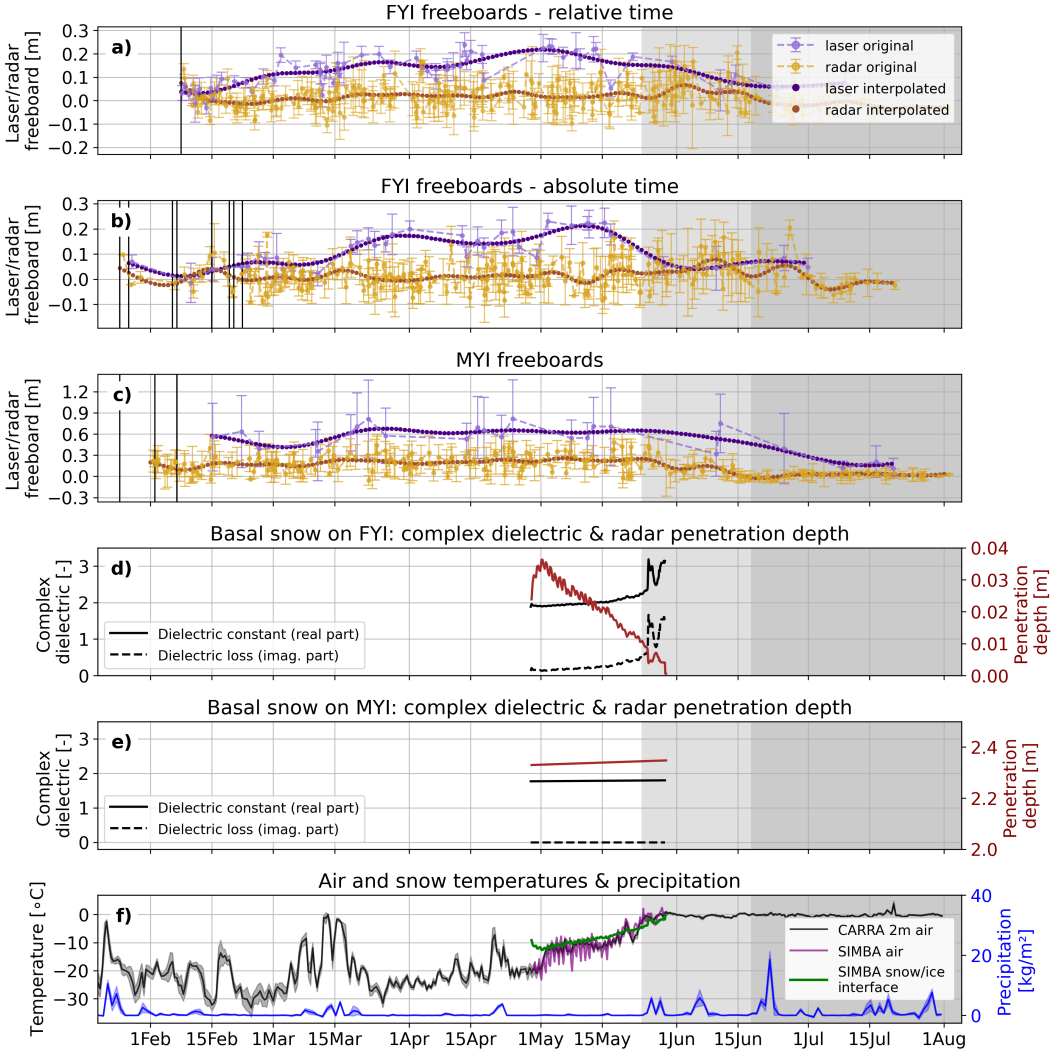

Figure 6. Panels (a), (b), (c): time series of laser and radar freeboards over FYI (relative and absolute time) and MYI, respectively, showing original samples (median + IQR) as well as daily interpolated values. Black vertical lines mark the timestamps tracking starts for individual ROIs. Note the difference in scales between the y-axes of FYI and MYI plots. Panels (d) and (e): modeled complex dielectric constant and radar penetration depth for basal snow on FYI and MYI, respectively. Panel (f): atmospheric conditions. The background colors highlight the different seasons: winter–melt onset–advanced melt.

This can be attributed to the more varied and deformed ice present in the MYI class, compared to only very smooth level ice in the FYI class. The transition towards melt onset (day 105–135) and advanced melt (day 135+) is characterized by increasingly narrow radar freeboard distributions, in combination with lower radar freeboard values. The laser freeboards maintain a large

https://doi.org/10.5194/egusphere-2026-1662
Preprint. Discussion started: 26 March 2026

spread, but the mode clearly shifts towards lower values. Over the entire time series the laser distributions have a large IQR and positive skew, with the long tail representing the fraction of (heavily) deformed ice.

Generally speaking, the freeboard distributions derived from CS-2 and S-3 are in good agreement considering median freeboard and shape of the distribution for both ice types; confirming that freeboards from both sensors can be used interchangeably. Figure B1 in the Appendix provides key statistics of the distributions over time. This figure shows that generally both the laser and radar distributions of MYI have a higher median and IQR than the FYI distributions. Meanwhile, a positive skew and Kurtosis (samples are closely centered around the mean with only few outliers) seem characteristic of a typical laser freeboard distribution, regardless of ice type. In contrast, the radar freeboard distributions are typically less skewed and have a low kurtosis (broader, flatter distributions).

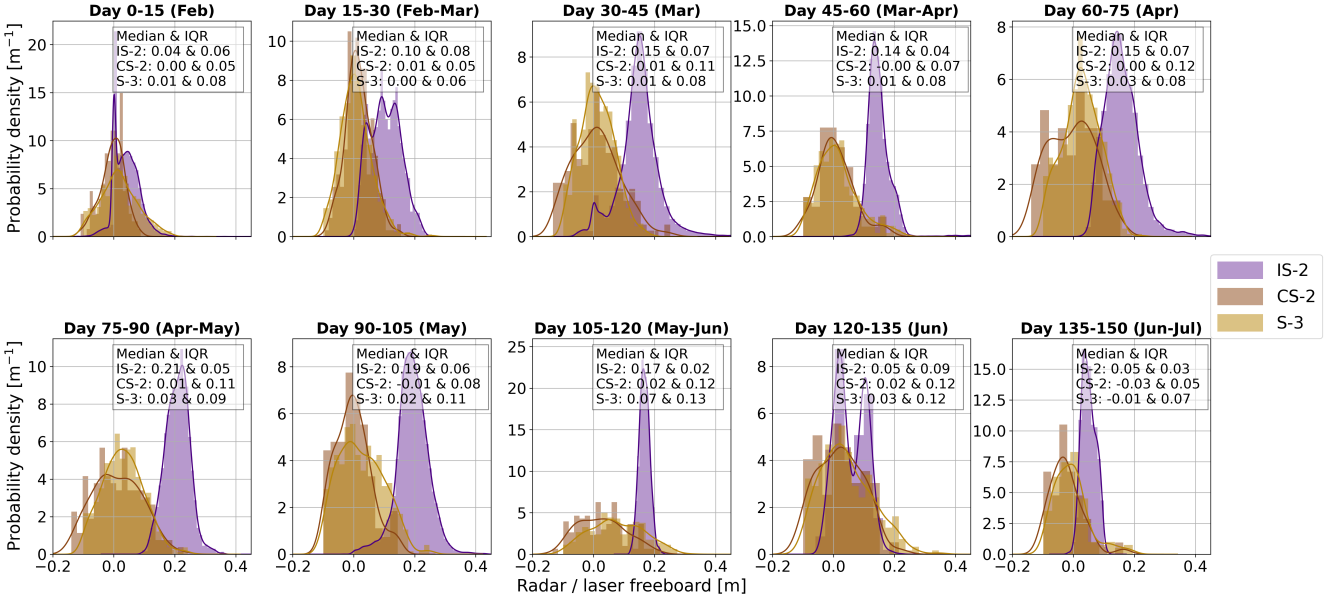

Figure 7. The evolution of laser and radar freeboard distributions at 15-day intervals for FYI.

5.3 Dielectric properties of the basal snow layer in the transition from winter to melt onset

Panels (d) and (e) in Fig. 6 show the modeled complex dielectric of the basal snow layer for a saline (FYI) snow cover and fresh (MYI) snow cover, respectively. In early May the basal snow temperatures are around -12°C and the dielectric has similar values for both saline and fresh snow. Throughout May the basal snow temperatures follow an ∼linear positive trend. The dielectric of saline (FYI) snow has a slight positive linear trend in the first half of May followed by an exponential rise in the second half of May. The transition to exponential growth coincides with basal snow temperatures rising above -7 °C. In the range -5 to 0°C the complex dielectric is very sensitive to minor temperature changes, as a small temperature shift in this range

https://doi.org/10.5194/egusphere-2026-1662
Preprint. Discussion started: 26 March 2026

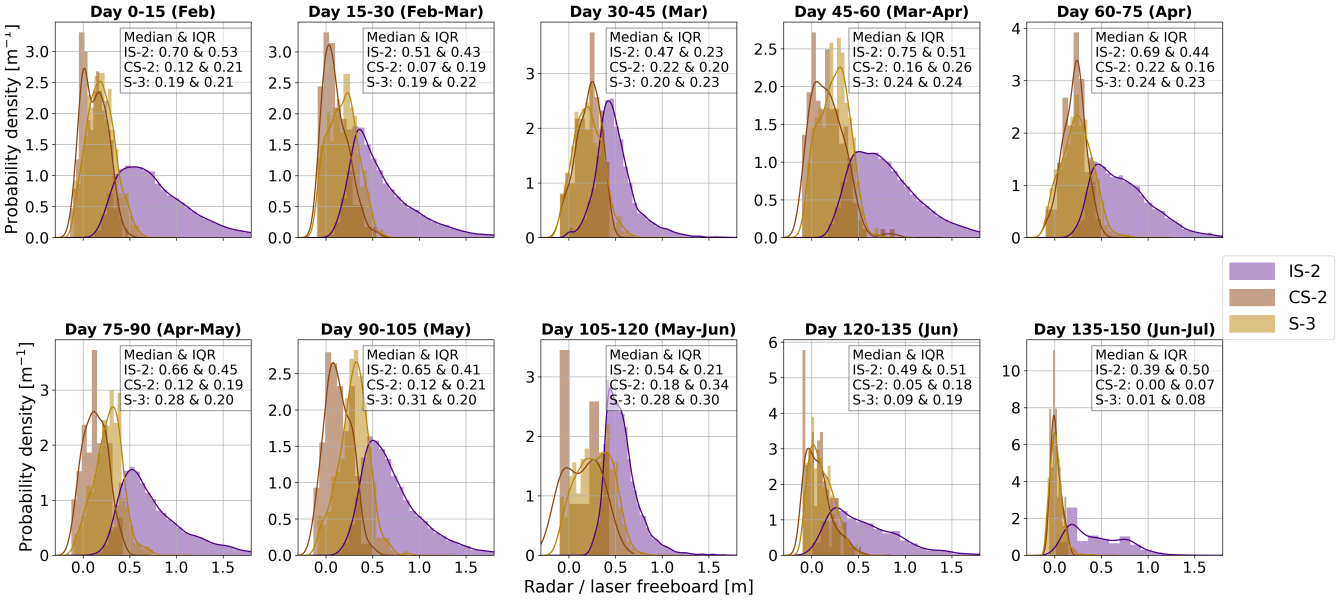

Figure 8. The evolution of laser and radar freeboard distributions at 15-day intervals for MYI. Note the scale difference on the x-axis compared to the FYI distributions in Fig. 8.

translates to a large change in liquid water content if the snow is saline. Meanwhile, the complex dielectric of fresh (MYI) basal snow remains constant across the observed range of snow temperatures, i.e. -15 to 0°C.

The increasing values of the complex dielectric constant result in reduced Ku-band radar penetration depth into the 4 cm thick basal snow layer. However, in contrast to the nonlinear increase in the dielectric constant, the radar penetration depth reduces at a more constant rate throughout the entire month of May, going from ∼4 at -10°C to 0 cm penetration depth at 0 °C. This implies that, theoretically, there is full penetration of radar waves in the saline basal layer in early May, followed by a rapid transition towards no penetration right after melt onset in late May. Radar penetration in the fresh snow on MYI is stable and in the order of meters, meaning that theoretically the radar waves fully penetrate the basal snow layer as long as snow temperatures are below the freezing point.

5.4 Seasonal evolution of radar waveform parameters

The evolution of a selection of Ku-band radar waveform parameters and C-band SAR backscatter coefficient is visualized in Fig. 9. From top to bottom the following parameters are shown: leading edge width (LEW), pulse peakiness (PP), radar backscatter coefficient (σ_0) in decibels for nadir Ku-band and side-looking SAR C-band. Parameters over MYI are stable throughout winter, with a low variance on the PP and σ_0, and higher variance on the LEW. The latter highlights that the MYI is significantly rougher than the FYI, and that the roughness varies across ROIs. Over FYI, the first 2–3 months after ice formation all parameters have distinctly different values than over MYI. Then, between 1–15 March, a sharp transition happens towards

https://doi.org/10.5194/egusphere-2026-1662
Preprint. Discussion started: 26 March 2026

values closer to those observed over MYI. Afterwards, FYI parameters remain stable for a month before tending even closer to values observed over MYI towards the end of winter. More specifically, the LEW over FYI increases throughout the winter while the PP decreases. Since the ice is immobile and not deforming on the meters-scale, this is indicative of changes in the small-scale surface roughness of the ice and/or changes in the overlying snow cover. Interestingly, the LEW and its variance are very low over newly-formed sea ice, but increase significantly over the winter period. During melt onset the FYI parameters continue to evolve along the winter trends, while MYI parameters make a sudden jump in the transition towards advanced melt. The FYI parameters make the same jump with a 2 week delay (i.e. at the start of July) - well into advanced melt. Note how the FYI waveform parameters in advanced melt reach values similar to the ones seen at the time of initial ice formation.

The backscatter from SAR and altimetry should not be expected to correlate very closely, due to the different sensing geometries and frequencies, but the observations reveal similar patterns between frequencies. The seasonal evolution of C-band SAR backscatter over Arctic sea ice has been extensively studied, but the evolution of nadir Ku-band backscatter from satellite observations of the same ice has, to our knowledge, not been shown before with this temporal resolution. For FYI the ∼2 week-long ice formation period is characterized by a U-shaped variation in backscatter at both C- and Ku-band. The effects around ice formation are smeared out here because the parameters are visualized in absolute time. The backscatter values decrease and stabilize after ∼2 months at C-band, while Ku-band backscatter keeps decreasing throughout the winter period, with a steep decline from ∼30 to 20 dB between 15 February–15 March, followed by a stable period and then slower decline towards 15 dB right before melt onset. At melt onset the backscatter over FYI rises in C-band and remains at similar values during advanced melt. At Ku-band the backscatter further decreases during melt onset before making a sudden jump from 10 to 30 dB in the advanced melt period (early July). Over MYI the backscatter coefficients are relatively constant during winter for both frequencies, with the SAR C-band backscatter ∼6 and 12 dB higher over MYI than FYI for HH- and HV-polarization, respectively, and in contrast nadir Ku-band ∼15 dB higher over FYI than MYI. At melt onset C-band backscatter for MYI drops and stabilizes at similar values as for FYI, while Ku-band backscatter first remains low and then shows a sudden increase from ∼5 to 30 dB in the transition towards advanced melt, so ∼2 weeks earlier than the jump observed over FYI.

5.5 Seasonal evolution of dual-altimetry snow depth & sea ice thickness

Figure 10 shows the temporal evolution of laser and radar freeboards in absolute time, and derived SD and SIT for FYI (panels (a), (b), (c)) and MYI (panels (e), (f), (g)), as well as cumulative precipitation and snow height equivalent (panels (d) and (h)). The SD and SIT are derived in two different ways: from LaKu dual-altimetry and from the snow/ice model.

Over FYI the LaKu SD is ∼0 cm when the ice forms, but it should be noted that small negative values at the start of the time series - due to radar freeboards being higher than laser freeboards - were set to zero to avoid using physically impossible snow depths in the SIT calculations. The SD increases stepwise throughout winter until reaching a maximum around 15 May with a median SD of 18 ± 6 cm. The major precipitation events (panel (d)) are reflected in the LaKu snow accumulation, albeit sometimes with a delay of 7–15 days, which is due to the interpolation scheme used to create the freeboard time series at daily resolution. The modeled SD is below the LaKu SD during most of the winter period and predicts a more continuous snow accumulation compared to the LaKu product. The higher snow accumulation rate over young ice might be caused by wind

https://doi.org/10.5194/egusphere-2026-1662
Preprint. Discussion started: 26 March 2026

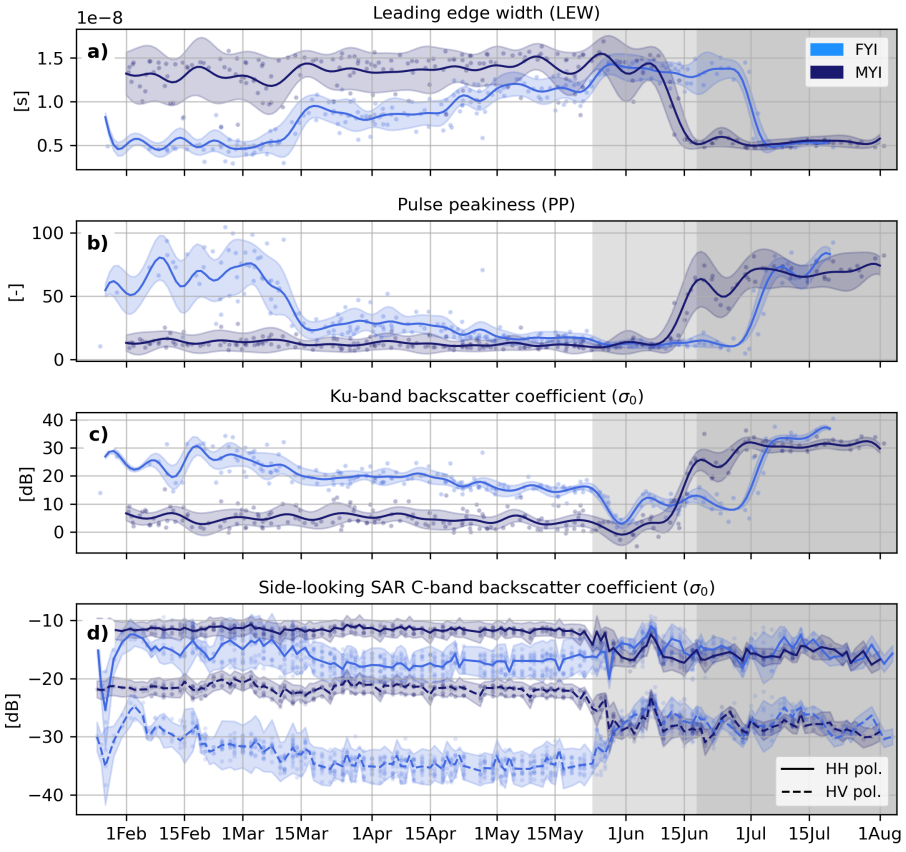

Figure 9. Seasonal evolution of a selection of radar waveform parameters over FYI and MYI (panels (a), (b), (c)), and seasonal evolution of the C-band SAR backscatter coefficient of the side-looking Sentinel-1 SAR sensor, for both ice types and imaging polarizations (panel (d)).

redistribution of snow, which is not well captured in the snow/ice model. The in situ data measured on 29 April revealed a SD of 18 cm, which is 5 cm higher than the median LaKu SD on that day, but within the IQR. Furthermore, the cumulative snow height equivalent from reanalysis (14 cm) is in good agreement with the maximal LaKu SD (18 ± 6 cm) reached near the end of the winter period.

The median FYI SIT (panel (c)) starts at ∼0.4 m, due to the initially high radar freeboards, then quickly drops down to 0 m before steadily increasing to a maximum of ∼0.9 m in early May. The in situ measurements on 29 April revealed a SIT of 0.92 m, which is in good agreement with the dual-altimetry SIT of ∼0.8±0.5 m. The modeled SIT shows a steeper ice growth rate of 1.3 cm day^{-1} compared to the dual-altimetry of 1 cm day^{-1}, leading to a difference of ∼0.25 m in early May, and a maximal difference of ∼0.4 m in the middle of May. The higher ice growth rate is a direct consequence of the lower volume of modeled snow accumulation up to mid-April, leading to less insulation between the cold atmosphere and the underlying ocean and therefore increasing thermodynamic ice growth.

https://doi.org/10.5194/egusphere-2026-1662
Preprint. Discussion started: 26 March 2026

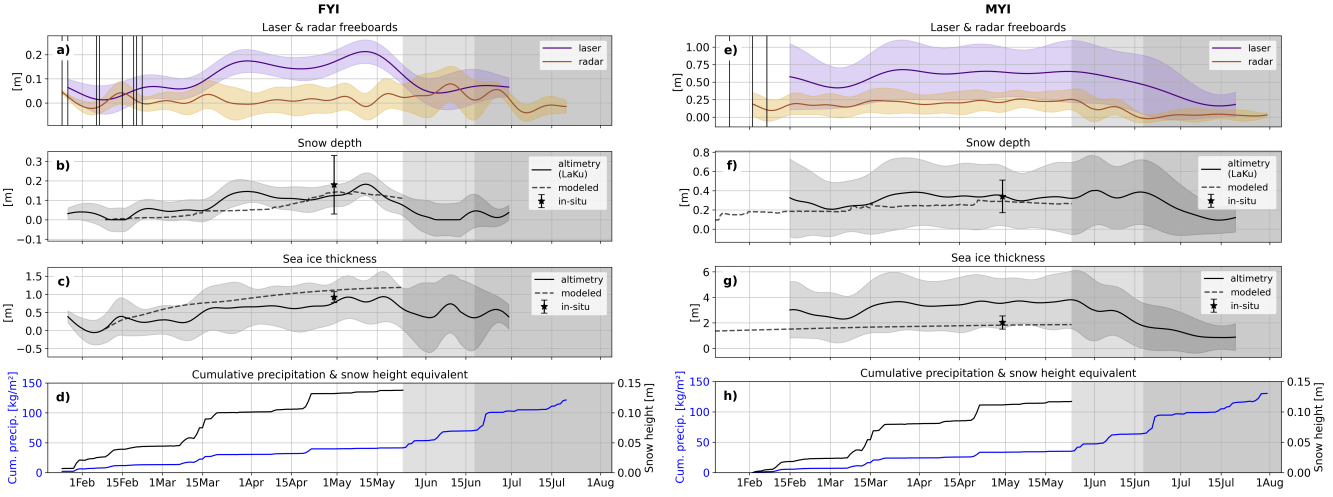

Figure 10. Panels (a), (b), (c) (FYI) and (e), (f), (g) (MYI): freeboards, snow depth, and sea ice thickness derived from dual-altimetry observations, numerical modeling, and in situ measurements. Panels (d) (FYI) and (h) (MYI): cumulative precipitation and corresponding snow height equivalent from CARRA reanalysis.

Panels (e), (f), (g), and (h) in Fig. 10 show the same variables over MYI. Note the large scale differences on the y-axis between the FYI and MYI plots. The LaKu snow depth over MYI (panel (f)) varies between ∼0.3–0.4 m over the winter period, apart for a short time around 1 March when it decreases down to 0.2 m. The modeled snow depth is on average 5–10 cm below the LaKu snow depth during the winter period; a similar offset as seen over FYI. LaKu snow depth is in very good agreement with the in situ measured depth of 0.34 cm in late April. During melt onset the LaKu snow depth remains high, as both the laser and radar freeboards decline at similar rates, and precipitation events are potentially still falling as snow. Advanced melt is marked by a rapid decline of -1.2 cm day^{-1} in snow depth.

Altimetry-derived SIT for MYI (panel (g)) is relatively stable throughout the winter period at ∼3.7 m, followed by an approximately linear decline in melt onset and early advanced melt, at a rate of -6.6 cm day^{-1}. The modeled SIT is 1.5–2 m thinner than the altimetry-derived values, and so is the in situ SIT measured on April 29. The ice growth rate during winter is 1 cm day^{-1} in the altimetry-derived product compared to 0.2 cm day^{-1} in the modeling output, even though the altimetry-derived SIT is significantly thicker and has a deeper snow cover. Compared to FYI, a major difference is apparent in the trends at melt onset when SIT rises over FYI while it decreases over MYI.

6 Discussion

For both ice types and during most of the winter, the time series suggests that the retracked heights at Ku-band frequency correspond to locations well below the air/snow interface, and likely close to the snow/ice interface. This finding is consistent with the assumption that radar waves penetrate through cold snow and that the dominant return originates from surface scattering at

https://doi.org/10.5194/egusphere-2026-1662
Preprint. Discussion started: 26 March 2026

the snow/ice interface. However, short-term periods with elevated radar freeboards are observed at different moments in both the winter and melt season. Temperature is a key driver of changes in the dielectric snow properties that affect the propagation of Ku-band radar waves, because it governs the liquid water content in the snow (Nandan et al., 2020). We therefore discuss the interaction of radar waves with snow in cold versus warm conditions and examine the implications for radar freeboard retrievals, as well as dual-altimetry snow depth and ice thickness products. The distinction between "cold" and "warm" conditions cannot be made through a fixed temperature threshold because other snow characteristics, such as salinity, influence the dielectric snow properties. In the time series studied here, we define the transition from "cold" to "warm" conditions as an increase in air temperature to above -10°C.

6.1 Radar freeboard retrievals in cold conditions

We observe that the principal scattering height of laser and radar observations is distinctly different throughout the entire winter period, both for FYI and MYI. Median laser freeboards are consistently higher than median radar freeboards, with little overlap between the IQR envelopes - except for FYI in the first week of ice formation. This indicates that, under cold conditions, the retracked heights at Ku-band frequency correspond to locations below the air/snow interface. If no competing biases are present, this implies that the Ku-band radar waves at least partly penetrate into the snow cover. By careful analysis of the time series we identify three situations where the Ku-band radar freeboards seem overestimated in cold conditions, i.e. the retracked heights do not trace the snow/ice interface but a location higher up in the snow.

Newly-formed ice At the moment of ice formation we expect the laser and radar returns to produce equally low freeboards, as there is no snow cover yet and both sensors should observe the same surface. However, we observe spuriously increased freeboards for both frequencies. High Ku-band freeboards are notably seen only in the Northern FYI ROIs (not shown here), but impact the full FYI area-averaged freeboards in the first 1–2 weeks after ice formation. As there is no snow cover on the ice yet that can bias the freeboard retrievals, we suspect this bias to originate from : (i) ocean wave effects, (ii) the retracking process and/or (iii) ice properties during formation. At the very onset of ice formation, the high LEW and low PP values suggest ice forming in ocean swells (Zhu et al., 2917). On a slightly longer timescale, the Ku- σ_0 time series show a U-shaped change over FYI in the weeks of ice formation (25 Jan–20 Feb), which likely represents the formation and decay of frost flowers on the new ice. These features significantly increase the roughness at centimeter-scale and thus increase scattering at the air/ice interface, which leads to broader waveform returns (Landy et al., 2020). We observe this effect in the radar waveform parameters: periods of lower Ku-band backscatter are accompanied by lower PP and higher LEW (note that the effect is smeared out since the waveform parameters are displayed in absolute time). The broader waveforms might displace the tracking point up from the air/ice interface, causing radar freeboards to be biased high.

Saline basal snow layer The radar modeling results suggest that Ku-band waves only penetrate 3–4 centimeters into snow with salinity values in the range 1–6 PSU for air temperatures in the range -15 to -10 °C and snow ∼-10 °C. The 3–4 cm distance roughly corresponds to the average height above the snow/ice interface up to where saline snow was observed in situ, although Arctic-wide saline snow can be found up to 6–8 cm and at salinities in the range 0–20 PSU (Nandan et al., 2017). So, in case of a thick saline basal layer ($>$ 4cm) and/or a highly saline basal layer (S$>$6 PSU), the retracked height might

https://doi.org/10.5194/egusphere-2026-1662
Preprint. Discussion started: 26 March 2026

not correspond to the location of the snow/ice interface but a location higher up in the snow, even in cold temperatures. This positive bias would be caused by increased radar wave absorption and/or volume scattering in the basal snow layer, which reduces the relative contribution of the snow/ice surface reflection in the detected waveform (Zhou et al., 2026). Figure 11 shows modeled brine volume and radar penetration depth into the basal snow layer for a range of typical snow temperature and salinity values found in snow on Arctic sea ice.

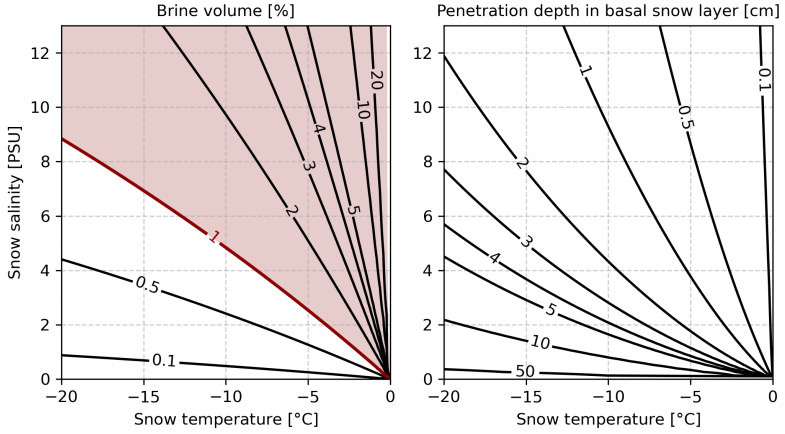

Figure 11. Brine volume and Ku-band radar penetration depth into the basal snow layer for a range of typical Arctic snow temperature and salinity values, assuming a snow density of 350 kg/m^3. Red shading is applied where combinations of temperature and salinity lead to a brine volume exceeding 1%, which is empirically associated with high likelihood of biased radar freeboards.

Thick snow cover The radar waveform is composed of the joint returns from surface scattering at the air/snow and snow/ice interfaces, plus in some cases snow volume scattering and surface scattering from internal snow layers. Previous studies have pointed out that thick snow covers (>20 cm) can displace the tracking point towards the altimeter and bias radar freeboards high, because returns from the air/snow interface significantly broaden the waveform (Kwok, 2014; Ricker et al., 2015). In this light, we suspect the thick snow cover on the MYI in this study (> 30cm) to be biasing the radar freeboards high. This would contribute to the discrepancy between the altimetry-derived SIT of ∼3.7 m and the in situ measured SIT of 2 m. The actual SIT most likely was in between the in situ and altimetry-derived values, as the in situ SIT obtained from manual transects tends to be underestimated. For practical reasons, manual transects with the GEM and Magnaprobe devices are not feasible over heavily deformed ice, and only one transect of 1 km total was made over MYI, whereas our polygons cover 1340 km^{-2}; well beyond the in situ sampling sites. Hence, the thickest ice and snow may not be well captured in the in situ measurements. Even though we suspect a high bias over the MYI areas, the difference between the laser and radar freeboard time series reveals that the retracked heights at Ku-band frequency correspond to locations well below the air/snow interface, with at least 60% penetration into the snow during winter.

https://doi.org/10.5194/egusphere-2026-1662
Preprint. Discussion started: 26 March 2026

6.2 Radar freeboard retrievals in warm conditions

We observe warm conditions at two distinct moments in the time series: during the winter warming events and during melt onset and advanced melt. The warming events are a temporary change from the cold winter baseline conditions, while the transition from winter to melt marks a shift of regimes that comes with more significant and lasting physical changes in the snow and ice. We therefore discuss both cases separately, even though some mechanisms are shared.

6.2.1 Warming event during winter

During the warming events around 15 March and 20 April, air temperatures are mainly in the range -10 to 0 °C and CARRA indicates ∼50 mm snowfall. We observe concurrent, temporary increases in radar freeboard, with MYI radar freeboards temporarily increasing by 10 and 5 cm in response to 5 and 3 cm snow accumulation, respectively. Over FYI the radar freeboards rise from ∼0 to 4 cm during the snowfall event of 15 March, but no significant freeboard increase is visible for the event in April. It is unlikely the freeboard rises are data artefacts, since they are all evident in several independent altimeter crossings from CS-2, S-3A and S-3B. At both occurrences, FYI waveform parameters drastically change, with LEW increasing while PP decreases, and the C-band backscatter over FYI drops by ∼5 dB. These findings indicate major geophysical changes in the snow cover over FYI. Interestingly, no significant changes are observed in the MYI waveform parameters and SAR backscatter, except for a small increase in LEW.

Strong snowfall Over both ice types the radar freeboards show a positive correlation to large winter snowfall events, i.e. radar freeboards slightly increase during the period of snowfall and stay heightened for ∼1 week afterwards before returning to pre-snowfall values. These observations contradict the common understanding that snow loading weighs the ice down, which should result in a decrease in radar freeboards (theoretically 0.54 cm decrease per cm snow accumulated (Nab et al., 2023)). The temporary increase in freeboards suggests that the principal radar scattering height is elevated up towards the altimeter during and right after periods of snowfall, which is in line with the findings of (Gregory et al., 2021; Nab et al., 2023). Snowfall events often coincide with warmer air temperatures, but the freeboards tend to stay elevated longer than the temperatures do.

The temporary elevation of the principal radar scattering height is suspected to, at least partly, come from changes in the roughness of the air/snow interface (Nab et al., 2023), at scales corresponding to snow features (dunes, drifts) and micro topography down to the radar wavelength (mm–cm roughness) (Landy et al.). Additionally, wind packing might increase the density of the upper snow layers. Most snow pits sampled in situ in late April had a dense upper half and softer bottom half structure, confirming wind packing happened in our study region. These surface roughness and snow density changes can redress the balance of Ku-band radar scattering between snow/ice and air/snow interfaces, since a change in the dielectric contrast across the air/snow interface or smoothening of the radar roughness could enhance scattering from the snow surface (Landy et al.). This could be caused by wind redistribution of snow and snow property changes during a storm (Nab et al., 2023; Nandan et al., 2023).

Notably, the waveform parameters over FYI show an increase in LEW and decrease in PP and Ku backscatter during the major snowfall events in mid-March and late April, indicating the radar waveform broadens in direct response to snow

https://doi.org/10.5194/egusphere-2026-1662
Preprint. Discussion started: 26 March 2026

accumulation and snow surface changes, as was also found in (Khvorostovsky et al.). An enhanced radar return from the air/snow interface relative to the snow/ice would broaden the detected waveform sampled at the satellite range resolution (47 cm). The waveform parameters do not return to pre-snowfall values afterwards, indicating that lasting physical changes are introduced in the snow cover during a strong snowfall event, but the radar freeboards do return. Interestingly, the MYI waveform parameters do not change in response to strong snowfall, except for a small increase in LEW. Compared to the FYI, the ice surface of MYI is very rough on large scales and very heterogeneous within the altimeter footprint. As a result, the returns from the snow/ice interface likely override the effects of changes in either snow surface roughness or internal snow properties over the MYI during storms.

Saline basal snow layer The relative freeboard bias observed in response to snowfall on MYI is much smaller compared to the bias over FYI (65 vs 400 % increase in freeboard), suggesting the presence of another mechanism that amplifies the effect over FYI. Snow on FYI typically has a saline bottom layer and a rise in temperature increases the brine volume fraction in this layer, even at temperatures below freezing point. Increased brine in the basal snow layer shifts it into the pendular saturation regime where water is contained in isolated pockets around the ice grains (Denoth, 1999), assuming that the microstructure of brine-wetted snow is similar to the microstructure of wet snow. Liquid water has a much higher dielectric loss factor than ice, leading to strong microwave absorption even at small brine volume fractions (Barber and Fung, 1998). In the presence of depth hoar crystals (which were observed in every sampled snow pit), the brine might coat the crystals and turn them into major scatterers at Ku-band frequency (Barber and Fung, 1998). This effect could shift the principal radar scattering location up toward the altimeter and lead to overestimated radar freeboards (Nandan et al., 2017). However, the total absorption or volume scattering directed away from the radar needs to be high enough to overpower the quasi-specular reflection that is commonly observed for peaky FYI altimeter echoes and that is thought to originate from the relatively smooth snow/ice interface (De Rijke-Thomas et al., 2023). A more likely alternative is that the enhanced radar wave absorption in the saline snow layer suppresses the reflection from the snow/ice interface, thereby allowing the air/snow interface reflection (or snow internal interface reflections) to contribute significantly to the detected waveform, which biases the retracked freeboards high. The latter theory implies that the dominant radar backscatter originates from the interfaces rather than from snow grains in or above the basal layer, and is more consistent with in situ nadir Ku-band radar studies that mainly observe sharp peaks at the key interfaces (Willatt et al., 2011; Stroeve et al., 2020). This additional bias introduced by saline snow in warmer periods also supports the satellite-based findings of (Nab et al., 2023) that CS-2 radar freeboard sensitivity to air temperature seems stronger over FYI than MYI.

We conclude that the radar freeboard increase observed over FYI during warming events is likely the combined result of snow accumulation, changes in the snow surface roughness, and increased brine volume in the basal snow layer. This can lead to (i) increased volume scattering within the snow cover, and/or (ii) increased surface scattering at the air/snow interface, and/or (iii) increased microwave attenuation in the saline basal snow layer. The detected waveform is broadened as a result of the two-way radar attenuation inside the basal snow layer, which reduces the strength of the return from the snow/ice interface, in combination with either relatively or absolutely larger contributions from snow volume and snow surface scattering. The radar freeboard increase is temporary, while changes in the waveform parameters are more permanent. We attribute this to the

https://doi.org/10.5194/egusphere-2026-1662
Preprint. Discussion started: 26 March 2026

fact that snow surface roughness and density/hardness changes are more long-lasting, while a brine volume increase reverses when temperatures drop again after a warming event. Generally speaking, periods of biased radar freeboards are short-term during the winter period - making up only ∼15% of the time.

6.2.2 Melt season

At the start of melt onset (24 May) the laser and radar freeboards start dropping for MYI. Over FYI, however, radar freeboards rise while laser freeboards decline. This uptick in radar freeboards starts before melt onset, with the first elevated freeboards around 17 May, and lasts until 7 June. Radar freeboards rise by ∼8 cm in this time period, while air temperatures go from -10 to 0°C and snow temperatures from -8 to 0°C. Vertical snow temperature gradients from the SIMBA instrument reveal a transition period between mostly positive gradients to negative gradients between 16–22 May. This coincides with the appearance of the first elevated radar freeboards (individual crossings >0.1 m), but no clear changes are seen in the waveform parameters before melt onset. At the start of melt onset, a change in C-band backscatter is observed over both FYI and MYI, implying geophysical changes in the properties of the snowpack across the entire study region (Karlsen et al., 2024). However, we only observe a concurrent change in nadir Ku-band backscatter over FYI, not over MYI which is relatively stable, with the LEW also changing for FYI. So, the changes in the snowpack evident in C-band SAR only seem to manifest as a clear change in waveform parameters over FYI.

Saline basal snow layer The same mechanism as outlined for the warming event (Sect. 6.2.1) is also applicable at melt onset, i.e. warmer temperatures lead to increased brine volume fractions in the saline basal snow layer and hence increased microwave attenuation. In our time series, the rise in radar freeboards around melt onset starts when basal snow temperatures increase above -8°C. As can be seen in Fig. 11, this temperature corresponds to a brine volume fraction of 1% when assuming a salinity of 4.2 PSU (the median salinity of the FYI snow pits). Moreover, it corresponds to the eutectic temperature of sodium sulfate decahydrate (-8.2°C) (Geldsetzer et al., 2009). From the radar freeboard observations in the FYI time series and modeled saline snow dielectric constant, we conclude that snow with a brine volume above 1% is likely to introduce a positive bias in radar freeboards. This finding is in line with previous work reporting that at liquid water fractions above 0.01 the snow cover is dominated by the dielectric properties of the water over the properties of the dry snow (Howell et al., 2005). The higher the brine volume, the more likely and stronger the bias in radar freeboards.

Wet snowpack When temperatures remain positive for long enough, the entire snow column becomes saturated regardless of the presence of salts. This can lead to overestimated radar freeboards because Ku-band backscatter returns almost exclusively originate from the air/snow interface for a saturated snow pack (Howell et al., 2005). Large variability in retrieved freeboards on short time scales can occur due to diurnal thaw-freeze cycles that result in large differences in liquid water content during the day and night.

Superimposed ice The heightened radar freeboards at melt onset could also be caused by the formation of superimposed ice due to the refreezing of meltwater (Granskog et al.). This would imply that the observed freeboards are not biased high, but in fact physically rise if we define the sea ice as including the superimposed ice. However, this mechanism would be likely to effect both FYI and MYI, although not necessarily at the same time due to differences in the snow radiation budget (and thus

https://doi.org/10.5194/egusphere-2026-1662
Preprint. Discussion started: 26 March 2026

liquid water content) for snow packs of different depth, but we do not observe any freeboard increase during melt over MYI. We therefore conclude that there was likely no superimposed ice formation. Snow and ice thickness data from the SIMBA instrument that was deployed on MYI backs this up.

Melt ponds The drainage of melt ponds can cause a rapid increase in ice freeboard (Salganik et al., 2025), but in our time series the ice is still pond free at the time we observe the increase in radar freeboards. The SIMBA instrument indicates that there is no snow ablation until 29 May (no data afterwards) and Sentinel-2 optical imagery shows no ponds until at least 10 June 2022. The first image after a cloudy period shows ponded MYI on 27 June, while over FYI ponding increases between 30 June–3 July. We observe the first negative radar freeboards at the start of advanced melt, i.e. second half of June, which coincides with the appearance of the melt ponds over MYI. The ponds are highly reflective surfaces that dominate the radar echo and cause the retracker to overestimate the range (Armitage and Davidson, 2014), requiring specialized waveform classification and freeboard derivation algorithms (Braakmann-Folgmann et al., 2026). For MYI we see the first negative freeboards at the start of advanced melt, about one week after a large shift across all radar waveform parameters happens. Over FYI the pond onset timing seems delayed by two weeks compared to MYI, since we observe the same patterns in waveform parameters and freeboards but with a two week delay. The optical imagery confirms this. The earlier timing over MYI may be caused by liquid water forming in refrozen melt ponds at the base of the snowpack (from the previous summer), creating highly reflective targets to the radar.

We conclude that the heightened FYI radar freeboards during melt onset is a bias that is most likely caused by the saline snow, and potentially exacerbated by simultaneous snowfall. This theory is backed-up by the radar modeling results showing an exponential increase in the complex dielectric constant of saline snow when the brine volume fraction exceeds 0.01, i.e. 1%.

6.3 Implications for dual-altimetry snow depth and ice thickness retrievals from ice formation to melt

Our findings suggest that the assumption of full snow penetration at Ku-band frequency for SIT retrievals and dual-frequency altimetry snow depth retrievals is valid for ∼85% of the winter period (in this time series). Still, more in situ validation data is needed at different times throughout the season and at larger scales to fully confirm this. We have only one tie point for validation, but this is near the end of the snow accumulation and ice growth seasons so it at least integrates processes affecting the ice since formation. The LaKu snow depth is within a few centimeters of the modeled snow depth at the end of the winter season. However, the LaKu snow depth shows a more rapid increase in the first weeks after ice formation compared to modeled snow accumulation, which might be caused by wind redistribution of snow. These findings are in line with previous studies reporting considerable snow deposition on newly-formed ice, particularly in the Atlantic sector of the Arctic where large cyclones are more common (Landy et al.).

The short-term periods of biased radar freeboards observed at different moments throughout the winter and melt season impact the SD and SIT retrievals. The bias in laser and radar freeboards observed during the first week of ice formation leads to overestimated LaKu SD and SIT. It shows that correctly locating the retracking point on a waveform return over very smooth and thin ice (<20–30 cm) remains difficult, so care should be taken when deriving LaKu SD and SIT over areas with a high fraction of young ice, such as the marginal ice zone or polynyas. Apart from the first weeks after ice formation, our results show

https://doi.org/10.5194/egusphere-2026-1662
Preprint. Discussion started: 26 March 2026

that winter LaKu SD and SIT estimates obtained from Ku-band freeboards are reasonable as long as temperatures are cold. During winter, we adivse caution for LaKu snow depth and SIT estimates derived (i) over FYI with a saline snow cover during warmer periods, (ii) during and immediately after strong snowfall. In the time series studied here, these cases make up ∼15% of the winter period. In both cases Ku-band radar freeboards are likely to be biased high, resulting in underestimated snow depth and overestimated SIT values. The impact on SIT is largest, as a freeboard bias may magnify tenfold in the conversion to SIT if no other competing biases are present. The bias is particularly pronounced in the case of a winter warming event with snowfall over areas of FYI, because the different biases accumulate (although the extent to which they linearly add remains unclear). For the warming event observed in this study, the cumulative bias leads to a 400% increase in FYI radar freeboards in just a few days. This translates to an increase in SIT of ∼0.4–0.5m while derived snow depth remains constant, even though there is new snow accumulation in reality. Similar artifacts in derived snow depth and SIT are seen over FYI during melt onset, which leads to opposing trends in snow depth and SIT for FYI versus MYI. The lack of data in the advanced melt season bars the drawing of hard conclusions about LaKu snow depth and SIT at that time of the year; however, all freeboards are unrealistically thin over both ice types owing to melt pond biases (Landy et al., 2022).

7 Conclusions

We present a time series of laser and Ku-band radar freeboards from satellite altimetry over immobile regions of FYI and MYI ranging from mid-Winter to mid-Summer. For FYI this time series captures the entire seasonal cycle from ice formation to summer melt. Our analysis shows that the Ku-band radar freeboards over FYI trace the snow/ice interface during ∼85% of the winter time. This supports the validity of the assumption that Ku-band radar waves penetrate through the snow and that the dominant return at nadir originates from surface scattering at the snow/ice interface during winter time. Over MYI, the retracked heights correspond to locations well below the air/snow interface, with at least 60% penetration into the snow during winter. However, the data also provides evidence for short-term periods with heightened radar freeboards in the winter and the melt season, for both ice types. In the time series studied here, all cases of temporarily heightened Ku-band radar freeboards are biases in the retrievals rather than actual physical increases in freeboard, and these biases come from several sources. In most cases the bias coincides with specific atmospheric conditions that significantly change the physical and dielectric properties of the snow and thereby impact the retrieved freeboards. In particular, our results suggest that during winter the Ku-band radar freeboards tend to be biased high (up to 4 cm): (i) for ice with a saline snow cover during a warming event (brine volume fraction >1%), and (ii) during and immediately after strong snowfall events. Additionally, there is the potential for a positive bias over MYI with a thick snow cover (>30 cm), but this bias could not be reliably assessed from the data available in this study. Winter warming events are often accompanied by snowfall, leading to a cumulative bias for the areas with saline snow (i.e. most FYI in the Arctic). The cumulative bias can lead to a 400% increase in FYI radar freeboards in just a few days. In the period of melt onset in May/June, biased radar freeboards seem related to saline snow only, but biases are on average larger than during the winter period – with biases up to 10 cm, which may translate into a tenfold bias in sea ice thickness if no other competing biases are present. In the above-mentioned cases the overestimated Ku-band freeboards are caused by

https://doi.org/10.5194/egusphere-2026-1662
Preprint. Discussion started: 26 March 2026

specific snow dielectric properties and/or snow surface roughness effects that reduce the strength of the backscattered power from the snow/ice interface and allow the backscattered power from the air/snow interface to weigh more in the detected waveform. In a few other cases we identify a positive bias that seems to originate from algorithmic processing choices in the retracking process. Notably, the time series over FYI reveals that both the laser and radar freeboards are biased high over newly-formed ice; showing that accurately estimating freeboard over areas of thin and smooth ice (i.e. specular waveforms), that are potentially ocean wave-affected, remains challenging.

For the majority of the winter season (∼85%), our findings support the assumption of full snow penetration at Ku-band frequency for sea ice thickness retrievals, as well as for dual-altimetry snow depth retrievals, such as planned for the Copernicus Polar Ice and Snow Topography Altimeter (CRISTAL) mission (Kern et al., 2235). Though our results show evidence for short-term, high biases in Ku-band radar freeboards under specific atmospheric conditions and physical snow properties, correctly identifying the freeboard samples that are affected and quantifying the strength of the bias remains a topic of investigation. This raises the proposition for flagging Ku-band freeboard samples with '*probability of high bias*' based on ice type and air temperature: FYI and T>-10°C (saline snow cover in warm conditions). Dedicated validation campaigns will be needed to provide in situ snow depth and sea ice thickness data over the course of multiple weeks/months and at different times throughout the season. This could be achieved by deploying autonomous sea ice mass balance buoys on fast ice, as fast ice provides a more controllable test site that simplifies both the validation and the inter-comparison of different satellite sensors and observational frequencies.

Code and data availability. We intend to publish the data set of satellite laser and Ku-band radar freeboards, including auxiliary data such as snow and ice densities, precipitation, etc. This data set is currently in preparation. Any code necessary to use the data set will also be published with it.

Appendix A: Supplementary material related to Methods section

A1 SAR incidence angle normalization

Wide-swath SAR sensors acquire data over a large range of incidence angles (IA), with small IA at near-range and a continuous increase in IA across the swath. As a result, the radar backscatter intensities typically decrease with increasing IA for the same surface type. For backscatter values expressed in decibels, the rate of decrease across the swath, i.e. the slope, is approximately linear. The steepness of the slope depends on the surface roughness and dielectric constant of the material being imaged (Ulaby et al., 1981). When investigating the backscatter evolution in a SAR time series that is not made up of repeat pass images, it is important to correct the backscatter values for variations in IA (Yackel and Barber, 2000; Makynen et al., 2003). This process is referred to as *incidence angle normalization* and implies finding a slope estimate and subsequently mapping all backscatter values to a common IA using this slope estimate. Slope estimates for sea ice can either be taken from literature, or derived from the SAR data itself if enough images over the same surface are available. Here, we estimate slopes from the SAR time series,

https://doi.org/10.5194/egusphere-2026-1662
Preprint. Discussion started: 26 March 2026

as there are many images available and hence this should provide the most accurate slope estimate for the ice types inside our ROIs. We use the differencing method presented in (Geldsetzer and Howell, 2023) where a slope estimate is calculated for each successive pair of SAR images where the same ice is imaged at two different IA's. Following the method in (Geldsetzer and Howell, 2023), we estimate slopes per ice type for all pairs of images during freezing conditions and when the difference in IA is at least 7 °. The average slope estimate per ice type and polarization is reported in Table A1. These values are then used to project the backscatter values onto a common IA of 35°for the entire SAR time series, also in the melt season.

	FYI	MYI
HH pol.	-0.19	-0.15
HV pol.	-0.05	-0.12

Table A1. SAR backscatter slope estimates in dB/°, per polarization and ice type

A2 Removing false lead tie points in along-track radar altimetry observations

We overlay along-track freeboards on spatio-temporally coinciding SAR images. Temporal overlap is defined as a maximum time difference of 24 hours between the acquisition of a SAR image and an altimetry overpass. The visual aid of the SAR image helps to qualitatively interpret the altimetry data. It revealed, for example, that many radar waveform returns over the FYI ROIs in both CS-2 and S-3 were wrongly classified as leads, even weeks after the ice had initially formed. The FYI that forms inside the fast ice of Belgica Bank grows in extremely quiescent conditions and therefore has a very smooth surface. This causes the radar wave to reflect specularly and hence the waveforms look very similar to lead returns. Especially in the first weeks after ice formation, many of the waveform returns over the level ice are wrongly classified as leads. If the ice is still very thin, this is not immediately problematic, but as the ice grows thicker, the wrongly classified returns bias surrounding freeboard estimates low. Here, we wish to focus on the impact of snow and sea ice radar scattering biases on retrieved freeboards. So, as this issue appeared to be quite persistent in many of the ROIs in the time period weeks after ice formation (with a few misclassifications even up to April), we excluded all lead tie points within the fast ice and re-processed the CS-2 and S-3 freeboards using only lead tie points identified in the drift ice. This was achieved by applying a fast-ice mask before identifying lead tie points to calculate freeboard values. The fast-ice mask was manually delineated in QGIS by careful analysis of the SAR time series and overlaid ice charts from DMI where the fast-ice edge is marked (not shown here). To simplify the processing, only one fast-ice mask was outlined for the entire time period of February-April 2022, see Fig. 1. This was deemed reasonable as the fast ice edge does not move a lot in that time. To avoid excluding valid lead tie points in the drift ice, the mask was drawn rather conservatively and hence does not represent the exact fast-ice edge, but rather the part of the fast-ice that is completely immobile between February and April.

https://doi.org/10.5194/egusphere-2026-1662
Preprint. Discussion started: 26 March 2026

A3 Calibrating radar backscatter values across the CS-2 and S-3 sensors

The backscatter values obtained with the S-3 sea ice retracker have not been calibrated against backscatter from CS-2 and therefore a significant shift in backscatter is observed between both sensors, as can be seen in Fig. A1. Here, we align the S-3 backscatter values to the CS-2 ones using the 1-D Wasserstein distance in order to quantify the horizontal shift between the two distributions. The Wasserstein distance is calculated as defined in Eq. (A1), where u and v are the 1D empirical probability density distributions from which the cumulative distribution functions U and V are calculated. The Wasserstein distance is calculated using all S-3 and CS-2 backscatter values over the ROIs and is found to be 21.6 dB over FYI, 21.2 dB over MYI, and 21 dB over FYI and MYI ROIs together. As the shift is similar over FYI and MYI, the averaged value of 21 dB is used as correction factor for both ice types and is subtracted from the S-3 backscatter intensities such that they align with the CS-2 intensities. Lastly, the Wasserstein distance was also calculated over a larger area of the Øer Ice Barrier spanning $\sim$ 230x100 km to verify that the shifts calculated from the ROIs are representative for the wider region. The Wasserstein distance was 20.5 dB for the entire study area and hence we conclude that the 21 dB over the ROIs is representative.

$$D_1(u,v) = \int_{-\infty}^{+\infty} |U - V| \tag{A1}$$

The backscatter distributions are shown in Fig. A1 per ice type, and for both ice types together before and after alignment. We can see that the MYI distribution is bimodal, while the FYI distribution is unimodal. The left distribution for MYI represent the increased backscatter intensities in the melt season, while the right peak corresponds to the backscatter pre-melt. For FYI the returns of pre-melt and melt are not distinguishable because backscatter values pre-melt change as the newly-formed ice matures and partly fall in the same range of values as after melt. The distribution for FYI and MYI together is simply the combination of the individual distributions and the result is a multimodal distribution where the modes of FYI and MYI pre- and after melt are clearly visible.

A4 IS-2: custom freeboard derivation for increased coverage in lead-sparse areas

We re-processed all IS-2 freeboards in this manner to obtain better laser altimetry coverage over the ROIs. We validate the new freeboard values by comparing all sets of beams from intersecting tracks over the fast ice within a time interval of at most 10 days ($\simeq$ 240 hours). In order to gather enough samples, intersections are collected over an area of $\sim$ 230x100 km spanning across all ROIs in the time period 15 January–15 May 2022, i.e. when the fast ice is stable and relatively immobile. An intersection is defined from beam-to-beam between two tracks, so for example beam 1 from track A is compared to beam 3 from track B in the location where they spatially overlap. Both inter-beam and intra-beam comparisons are considered as intersections, as freeboard is a relative measure and hence inter-beam range biases cancel out. To get a statistical representation of the freeboard distributions at each intersection, all samples along both beams that are within a certain radius of each other are collected. We used search radii of 250, 500, and 1000 m, which led to search results with time lags of 34, 61, 130, 157, or 226 hours. An overview of the number of intersections for different time lags and search radii is shown in Fig. A2. The intersection

https://doi.org/10.5194/egusphere-2026-1662
Preprint. Discussion started: 26 March 2026

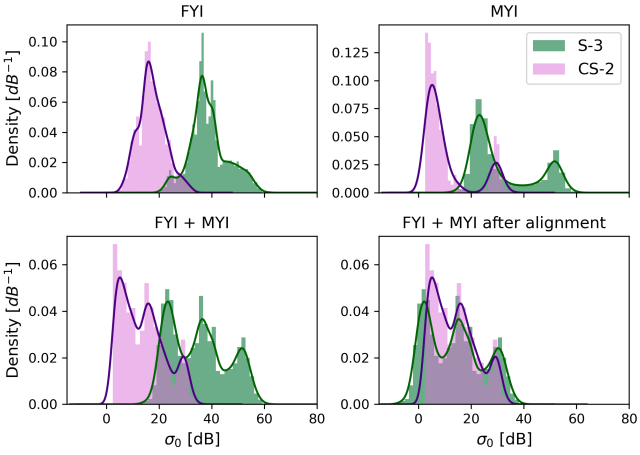

Figure A1.

Sigma nought backscatter distributions and kernel density estimates for CS-2 and S-3 per ice type (top row) and for both ice types together, before and after alignment (bottom row).

are then quality-filtered by two criteria: 1) the beam-to-beam difference in average small-scale surface roughness (calculated from the width of Gaussian fit on the photon height distribution) should be less than 0.1, and 2) at least 100 freeboard samples should be available per beam to ensure statistical representability. Intersections where the difference in surface roughness between both beams is more than 0.1 might indicate that both beams sampled a different ice surface, e.g. when the intersection covers both FYI and MYI. This is likely the reason why the amount of intersections for a radius of 1000 m is lower compared to 500 m at the 61 h time lag in Fig. A2. The absolute difference in laser freeboards at intersections, per time lag and search radius, is shown in Fig. A3. The median absolute difference in laser freeboards is consistently $\sim$ 5 cm, independently of search radius or time lag, with an exception for the intersections with a time lag of 157 hours where slightly higher differences are observed. The variance, however, increases with time lag, especially for the time lags larger than 130 hours ($\sim$ 5 days). The higher variance is expected at these time scales, as physical changes are more likely to have happened on the surface. The scatterplot of laser freeboard pairs in Fig. 3 shows correlation coefficients in the range 0.67–0.89. The lowest correlation is for intersections with a time lag of 130 hours, which is the group with the least amount of observations. The freeboards at this time lag have a narrow distribution centered $\sim$40cm, which results in a lower correlation coefficient than the distributions with a wider variance and more observations.

Appendix B: Supplementary results

https://doi.org/10.5194/egusphere-2026-1662
Preprint. Discussion started: 26 March 2026

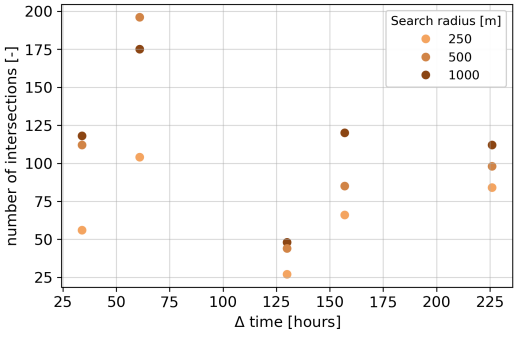

Figure A2. Number of intersections per search radius at five different time lags.

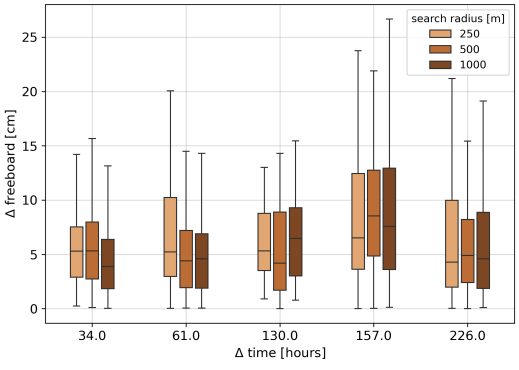

Figure A3. Boxplots showing the absolute difference in laser freeboards at intersections, for three different search radii at five different time lags.

https://doi.org/10.5194/egusphere-2026-1662
Preprint. Discussion started: 26 March 2026

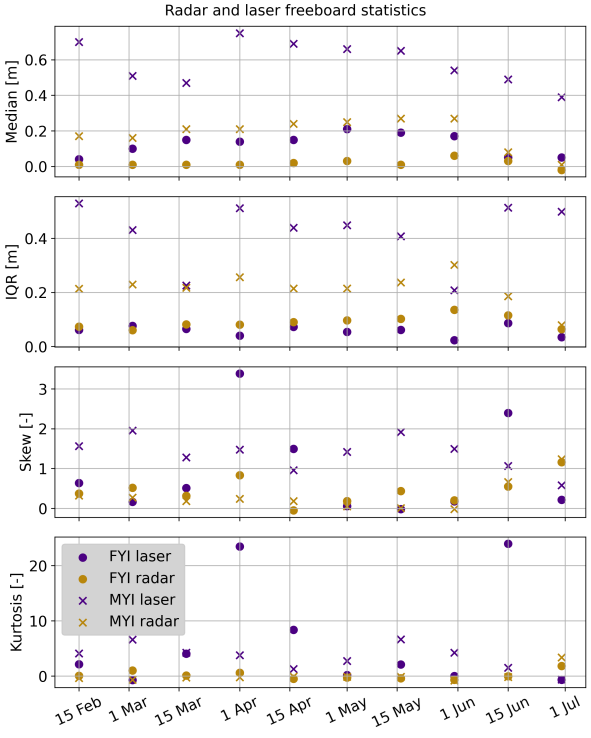

Figure B1. Laser and radar freeboard statistics for FYI and MYI at 15-day intervals.

https://doi.org/10.5194/egusphere-2026-1662
Preprint. Discussion started: 26 March 2026

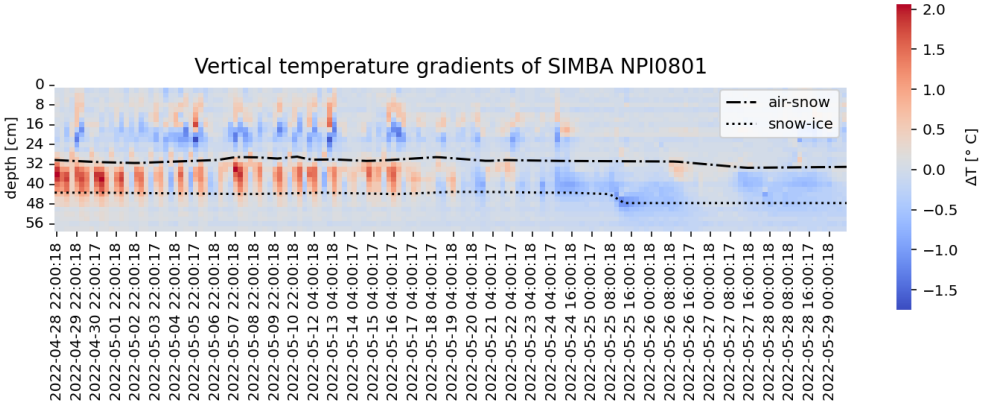

Figure B2. Vertical temperature gradients obtained from SIMBA instrument measurements between 28 April and 29 May 2022. Dashed lines indicate the air/snow and snow/ice interfaces derived from the heating cycle measurements.

https://doi.org/10.5194/egusphere-2026-1662
Preprint. Discussion started: 26 March 2026

Author contributions. Original idea and design of the study: JL, CT. Processing of remote sensing data: CT, JL. Processing of in situ data: CT. Radar modeling: CT. Snow/ice modeling: PI. Interpretation of results: CT, JL, RM. Preparation of the manuscript: CT, JL, RM, PI.

Competing interests. The authors declare that they have no conflict of interest.

Acknowledgements. The authors would like to thank Anthony Doulgeris and Wolfgang Dierking for the insightful discussions that helped in shaping this study, and Evgenii Salganik for processing the SIMBA data to derive the air/snow and snow/ice interfaces from the heating cycles. The presented work contains primary and altered Sentinel data products (@Copernicus data). Map coastline data copyrighted OpenStreetMap contributors and available from https://www.openstreetmap.org. CT, JCL and PI acknowledge support from the Norwegian Research Council (NFR) project DynAMIC (Detecting episodes of Arctic sea ice Mass Imbalance) under grant #343069 and from the CIRFA (Centre for Integrated Remote Sensing and Forecasting for Arctic Operations) partners and NFR grant #237906 and ESA through ESA contract RFP/3-17845/22/NL/FF/ab. JCL acknowledges further support from the ESA CRISTAL LEVel-2 procEssor prototype and R&D Sea Ice and Iceberg (CLEV2ER) project under grant #AO/1-11448/22/I-AG; the Forskning for god forvaltning av Polhavet (SUDARCO) project under the Fram Centre under grant #2551323; and the Summer Sea Ice in 3D (SI/3D) project from the European Research Council, ERC under grant #101077496.

https://doi.org/10.5194/egusphere-2026-1662
Preprint. Discussion started: 26 March 2026

References

Armitage, T. W. K. and Davidson, M. W. J.: Using the Interferometric Capabilities of the ESA CryoSat-2 Mission to Improve the Accuracy of Sea Ice Freeboard Retrievals, IEEE TRANSACTIONS ON GEOSCIENCE AND REMOTE SENSING, 52, 529, https://doi.org/10.1109/TGRS.2013.2242082, 2014.

Aublanc, J., Renou, J., Piras, F., Nielsen, K., Rose, S. K., Simonsen, S. B., Fleury, S., Hendricks, S., Taburet, N., D'Apice, G., Chamayou, A., Féménias, P., Catapano, F., and Restano, M.: Sentinel-3 Altimetry Thematic Products for Hydrology, Sea Ice and Land Ice, Scientific Data 2025 12:1, 12, 1–17, https://doi.org/10.1038/s41597-025-04956-3, 2025.

Bagnardi, M., Kurtz, N. T., Petty, A. A., and Kwok, R.: Sea Surface Height Anomalies of the Arctic Ocean From ICESat-2: A First Examination and Comparisons With CryoSat-2, Geophysical Research Letters, 48, https://doi.org/10.1029/2021GL093155, 2021.

Barber, D. G. and Fung, A. K.: The role of snow on microwave emission and scattering over first-year sea ice, IEEE Transactions on Geoscience and Remote Sensing, 36, 1750–1763, https://doi.org/10.1109/36.718643, 1998.

Barber, D. G., Reddan, S. P., and Ledrew, E. F.: Statistical characterization of the geophysical and electrical properties of snow on landfast first-year sea ice, Journal of Geophysical Research, 100, 2673–2686, https://doi.org/10.1029/94JC02200, 1995.

Beaven, S. G., Lockhart, G. L., Gogineni, S. P., Hosseinmostafa, A. R., Jezek, K., Gow, A. J., Perovich, D. K., Fung, A. K., and Tjuatja, S.: Laboratory measurements of radar backscatter from bare and snow-covered saline ice sheets, Remote Sensing, 16, 851–876, https://doi.org/10.1080/01431169508954448, 1995.

Braakmann-Folgmann, A., Landy, J. C., Dawson, G., and Ricker, R.: Enhanced neural network classification for Arctic summer sea ice, The Cryosphere, 20, 905–929, https://doi.org/10.5194/tc-20-905-2026, 2026.

Carret, A., Fleury, S., Di Bella, A., Landy, J., Lawrence, I., Kurtz, N., Laforge, A., Bouffard, J., and Parrinello, T.: A multi-frequency altimetry snow depth product over Arctic sea ice, Scientific Data 2025 12:1, 12, 1–20, https://doi.org/10.1038/s41597-024-04343-4, 2025.

Dai, A.: Temperature and pressure dependence of the rain-snow phase transition over land and ocean, Geophysical Research Letters, 35, 12 802, https://doi.org/10.1029/2008GL033295, 2008.

De Rijke-Thomas, C., Landy, J. C., Mallett, R., Willatt, R. C., Tsamados, M., and King, J.: Airborne Investigation of Quasi-Specular Ku-Band Radar Scattering for Satellite Altimetry Over Snow-Covered Arctic Sea Ice, IEEE Transactions on Geoscience and Remote Sensing, 61, https://doi.org/10.1109/TGRS.2023.3318263, 2023.

Denoth, A.: Wet snow pendular regime: the amount of water in ring-shaped configurations, Cold Regions Science and Technology, 30, 13–18, https://doi.org/https://doi.org/10.1016/S0165-232X(99)00007-5, 1999.

Dierking, W., Schneider, A., Eltoft, T., and Gerland, S.: CIRFA Cruise 2022. Cruise report., https://doi.org/10.5281/zenodo.7314066, 2022.

ESA: ESA CryoSat-2 Product Handbook Baseline E 1.0, https://earth.esa.int/eogateway/documents/20142/0/CryoSat-Product-Handbook-Baseline-E-draft.pdf/fc311af8-b926-cf59-5e3a-6b81942e262f, accessed: 2026-02-20, 2026.

Fierz, C., Armstrong, R. L., Durand, Y., Etchevers, P., Greene, E., McClung, D. M., Nishimura, K., Satyawali, P. K., and Sokratov, S. A.: The international classification for seasonal snow on the ground, 2009.

Fredensborg Hansen, R. M., Skourup, H., Rinne, E., Høyland, K. V., Landy, J. C., Merkouriadi, I., and Forsberg, R.: Arctic Freeboard and Snow Depth From Near-Coincident CryoSat-2 and ICESat-2 (CRYO2ICE) Observations: A First Examination of Winter Sea Ice During 2020–2022, Earth and Space Science, 11, e2023EA003 313, https://doi.org/10.1029/2023EA003313, 2024.

Geldsetzer, T. and Howell, S. E.: Incidence angle dependencies for C-band backscatter from sea ice during both the winter and melt season, IEEE Transactions on Geoscience and Remote Sensing, 61, 1–15, 2023.

https://doi.org/10.5194/egusphere-2026-1662
Preprint. Discussion started: 26 March 2026

Geldsetzer, T., Langlois, A., and Yackel, J.: Dielectric properties of brine-wetted snow on first-year sea ice, Cold Regions Science and Technology, 58, 47–56, https://doi.org/10.1016/J.COLDREGIONS.2009.03.009, 2009.

Granskog, M. A., Dodd, P. A., Divine, D., Gerland, S., Martma, o., and Leng, M. J.: Snow contribution to first-year and second-year Arctic sea ice mass balance north of Svalbard, https://doi.org/10.1002/2016JC012398.

Gregory, W., Lawrence, I. R., and Tsamados, M.: A Bayesian approach towards daily pan-Arctic sea ice freeboard estimates from combined CryoSat-2 and Sentinel-3 satellite observations, Cryosphere, 15, 2857–2871, https://doi.org/10.5194/tc-15-2857-2021, 2021.

Howell, S. E., Yackel, J. J., De Abreu, R., Geldsetzer, T., and Breneman, C.: On the utility of SeaWinds/QuikSCAT data for the estimation of the thermodynamic state of first-year sea ice, IEEE Transactions on Geoscience and Remote Sensing, 43, 1338–1350, https://doi.org/10.1109/TGRS.2005.846153, 2005.

Hughes, N. E., Wilkinson, J. P., and Wadhams, P.: Multi-satellite sensor analysis of fast-ice development in the Norske Øer Ice Barrier, northeast Greenland, Annals of Glaciology, 52, 151–160, https://doi.org/10.3189/172756411795931633, 2011.

Itkin, P. and Liston, G. E.: Combining observational data and numerical models to obtain a seamless high-temporal-resolution seasonal cycle of snow and ice mass balance at the MOSAiC Central Observatory, The Cryosphere, 19, 5111–5133, https://doi.org/10.5194/tc-19-5111-2025, 2025.

Itkin, P., Hendricks, S., Webster, M., von Albedyll, L., Arndt, S., Divine, D., Jaggi, M., Oggier, M., Raphael, I., Ricker, R., et al.: Sea ice and snow characteristics from year-long transects at the MOSAiC Central Observatory, Elem Sci Anth, 11, 00 048, 2023.

Jutila, A. and Haas, C.: C and K band microwave penetration into snow on sea ice studied with off-the-shelf tank radars, https://doi.org/10.1017/aog.2023.47, 2023.

Jutila, A., Hendricks, S., Ricker, R., Von Albedyll, L., Krumpen, T., and Haas, C.: Retrieval and parameterisation of sea-ice bulk density from airborne multi-sensor measurements, Cryosphere, 16, 259–275, https://doi.org/10.5194/TC-16-259-2022, 2022.

Kacimi, S. and Kwok, R.: Two Decades of Arctic Sea-Ice Thickness from Satellite Altimeters: Retrieval Approaches and Record of Changes (2003–2023), Remote Sensing 2024, Vol. 16, Page 2983, 16, 2983, https://doi.org/10.3390/RS16162983, 2024.

Karlsen, T., Johansson, M., Lohse, J., and Doulgeris, A. P.: Incidence angle dependency and seasonal evolution of L and C-band SAR backscatter over landfast sea ice, Annals of Glaciology, 65, e29, https://doi.org/10.1017/AOG.2024.30, 2024.

Kern, M., Cullen, R., Berruti, B., Bouffard, J., Casal, T., Drinkwater, M. R., Gabriele, A., Lecuyot, A., Ludwig, M., Midthassel, R., Navas Traver, I., Parrinello, T., Ressler, G., Andersson, E., Martin-Puig, C., Andersen, O., Bartsch, A., Farrell, S., Fleury, S., Gascoin, S., Guillot, A., Humbert, A., Rinne, E., Shepherd, A., Van Den Broeke, M. R., and Yackel, J.: The Copernicus Polar Ice and Snow Topography Altimeter (CRISTAL) high-priority candidate mission, The Cryosphere, 14, https://doi.org/10.5194/tc-14-2235-2020, 2235.

Khvorostovsky, K., Hendricks, S., and Rinne, E.: remote sensing Surface Properties Linked to Retrieval Uncertainty of Satellite Sea-Ice Thickness with Upward-Looking Sonar Measurements, https://doi.org/10.3390/rs12183094.

King, J., Skourup, H., Hvidegaard, S. M., Rösel, A., Gerland, S., Spreen, G., Polashenski, C., Helm, V., and Liston, G. E.: Comparison of Freeboard Retrieval and Ice Thickness Calculation From ALS, ASIRAS, and CryoSat-2 in the Norwegian Arctic to Field Measurements Made During the N-ICE2015 Expedition, Journal of Geophysical Research: Oceans, 123, 1123–1141, https://doi.org/10.1002/2017JC013233, 2018.

Kwok, R.: Simulated effects of a snow layer on retrieval of CryoSat-2 sea ice freeboard, Geophysical Research Letters, 41, 5014–5020, https://doi.org/10.1002/2014GL060993, 2014.

Kwok, R., Zwally, H. J., and Yi, D.: ICESat observations of Arctic sea ice: A first look, Geophysical Research Letters, 31, 2004.

https://doi.org/10.5194/egusphere-2026-1662
Preprint. Discussion started: 26 March 2026

Kwok, R., Kacimi, S., Webster, M. A., Kurtz, N. T., and Petty, A. A.: Arctic Snow Depth and Sea Ice Thickness From ICESat-2 and CryoSat-2 Freeboards: A First Examination, Journal of Geophysical Research: Oceans, 125, https://doi.org/10.1029/2019JC016008, 2020.

Kwok, R., Petty, A., Cunningham, G., Hancock, D., Ivanoff, A., Wimert, J., Bagnardi, M., and Kurtz, N.: Algorithm theoretical Basis document (ATBD) for sea ice products, ICESat-2 Algorithm Theoretical Basis Document, Version, 4, 2021.

Kwok, R., Petty, A., Bagnardi, M., Wimert, J. T., Cunningham, G. F., Hancock, D. W., Ivanoff, A., and Kurtz, N.: Ice, Cloud, and Land Elevation Satellite (ICESat-2) Project Algorithm Theoretical Basis Document (ATBD) for Sea Ice Products, version 6, NASA National Snow and Ice Data Center Distributed Active Archive Center (DAAC) data set, p. 9VT7NJWOTV3I, 2023.

Landy, J. C., De Rijke-Thomas, C., Nab, C., Lawrence, I., Glissenaar, I. A., Mallett, R. D. C., Hansen, R. M. F., Petty, A., Tsamados, M., Macfarlane, A. R., and Braakmann-Folgmann, A.: Anticipating CRISTAL: An exploration of multi-frequency satellite altimeter snow depth estimates over Arctic sea ice, 2018-2023, https://doi.org/10.5194/egusphere-2024-2904.

Landy, J. C., Petty, A. A., Tsamados, M., and Stroeve, J. C.: Sea Ice Roughness Overlooked as a Key Source of Uncertainty in CryoSat-2 Ice Freeboard Retrievals, Journal of Geophysical Research: Oceans, 125, e2019JC015 820, https://doi.org/10.1029/2019JC015820, 2020.

Landy, J. C., Dawson, G. J., Tsamados, M., Bushuk, M., Stroeve, J. C., Howell, S. E., Krumpen, T., Babb, D. G., Komarov, A. S., Heorton, H. D., Belter, H. J., and Aksenov, Y.: A year-round satellite sea-ice thickness record from CryoSat-2, Nature 2022 609:7927, 609, 517–522, https://doi.org/10.1038/s41586-022-05058-5, 2022.

Laxon, S.: Sea ice altimeter processing scheme at the EODC, International Journal of Remote Sensing, 15, 915–924, https://doi.org/10.1080/01431169408954124, 1994.

Laxon, S., Peacock, H., and Smith, D.: High interannual variability of sea ice thickness in the Arctic region, Nature 2003 425:6961, 425, 947–950, https://doi.org/10.1038/nature02050, 2003.

Laxon, S. W., Giles, K. A., Ridout, A. L., Wingham, D. J., Willatt, R., Cullen, R., Kwok, R., Schweiger, A., Zhang, J., Haas, C., Hendricks, S., Krishfield, R., Kurtz, N., Farrell, S., Davidson, M., Giles, K. A., Ridout, A. L., Wingham, D. J., Willatt, R., Cullen, R., Kwok, R., Schweiger, A., Zhang, J., Haas, C., Hendricks, S., Krishfield, R., Kurtz, N., Farrell, S., and Davidson, M.: CryoSat-2 estimates of Arctic sea ice thickness and volume, Geophys. Res. Lett, 40, 732–737, https://doi.org/10.1002/grl.50193, 2013.

Lohse, J., Taelman, C., Everett, A., and Hughes, N. E.: Automated Sentinel-1 sea ice type mapping and in-situ validation during the CIRFA-22 cruise, Annals of Glaciology, 65, e39, 2024.

Makynen, M., Manninen, A. T., Simila, M., Karvonen, J. A., and Hallikainen, M. T.: Incidence angle dependence of the statistical properties of C-band HH-polarization backscattering signatures of the Baltic Sea ice, IEEE Transactions on Geoscience and Remote Sensing, 40, 2593–2605, 2003.

Mallett, R. D.: A methodologically robust densification function for snow on multiyear Arctic sea ice, Journal of Glaciology, 71, https://doi.org/10.1017/JOG.2025.5, 2025.

Nab, C., Mallett, R., Gregory, W., Landy, J., Lawrence, I., Willatt, R., Stroeve, J., and Tsamados, M.: Synoptic variability in satellite altimeter-derived radar freeboard of Arctic sea ice, Geophysical Research Letters, 50, e2022GL100 696, 2023.

Nandan, V., Geldsetzer, T., Yackel, J., Mahmud, M., Scharien, R., Howell, S., King, J., Ricker, R., and Else, B.: Effect of snow salinity on CryoSat-2 Arctic first-year sea ice freeboard measurements, Geophysical Research Letters, 44, 10–419, 2017.

Nandan, V., Scharien, R. K., Geldsetzer, T., Kwok, R., Yackel, J. J., Mahmud, M. S., Rösel, A., Tonboe, R., Granskog, M., Willatt, R., et al.: Snow property controls on modeled Ku-band altimeter estimates of first-year sea ice thickness: Case studies from the Canadian and Norwegian Arctic, IEEE Journal of Selected Topics in Applied Earth Observations and Remote Sensing, 13, 1082–1096, 2020.

https://doi.org/10.5194/egusphere-2026-1662
Preprint. Discussion started: 26 March 2026

Nandan, V., Willatt, R., Mallett, R., Stroeve, J., Geldsetzer, T., Scharien, R., Tonboe, R., Yackel, J., Landy, J., Clemens-Sewall, D., Jutila, A., Wagner, D. N., Krampe, D., Huntemann, M., Mahmud, M., Jensen, D., Newman, T., Hendricks, S., Spreen, G., Macfarlane, A., Schneebeli, M., Mead, J., Ricker, R., Gallagher, M., Duguay, C., Raphael, I., Polashenski, C., Tsamados, M., Matero, I., and Hoppmann, M.: Wind redistribution of snow impacts the Ka-and Ku-band radar signatures of Arctic sea ice, The Cryosphere, 17, https://doi.org/10.5194/tc-17-2211-2023, 2023.

Panaretos, V. M. and Zemel, Y.: Statistical aspects of Wasserstein distances, Annual review of statistics and its application, 6, 405–431, 2019.

Ricker, R., Hendricks, S., Helm, V., Skourup, H., and Davidson, M.: Sensitivity of CryoSat-2 Arctic sea-ice freeboard and thickness on radar-waveform interpretation, The Cryosphere, 8, 1607–1622, https://doi.org/10.5194/tc-8-1607-2014, 2014.

Ricker, R., Hendricks, S., Perovich, D. K., Helm, V., and Gerdes, R.: Impact of snow accumulation on CryoSat-2 range retrievals over Arctic sea ice: An observational approach with buoy data, Geophysical Research Letters, 42, 4447–4455, https://doi.org/10.1002/2015GL064081, 2015.

Rösel, A., Farrell, S. L., Nandan, V., Richter-Menge, J., Spreen, G., Divine, D. V., Gallet, J.-C., and Gerland, S.: Implications of surface flooding on airborne thickness measurements of snow on sea ice, The Cryosphere Discussions, 2020, 1–27, 2020.

Salganik, E., Crabeck, O., Fuchs, N., Hutter, N., Anhaus, P., and Landy, J. C.: Impacts of air fraction increase on Arctic sea ice density, freeboard, and thickness estimation during the melt season, The Cryosphere, 19, 1259–1278, https://doi.org/10.5194/tc-19-1259-2025, 2025.

Schyberg, H., Yang, X., Køltzow, M. A. , Amstrup, B., Bakketun, , Bazile, E., Bojarova, J., Box, J. E., Dahlgren, P., Hagelin, S., Homleid, M., Horányi, A., Høyer, J., Johansson, , Killie, M. A., Körnich, H., Le Moigne, P., Lindskog, M., Manninen, T., Nielsen Englyst, P., Nielsen, K. P., Olsson, E., Palmason, B., Peralta Aros, C., Randriamampianina, R., Samuelsson, P., Stappers, R., Støylen, E., Thorsteinsson, S., Valkonen, T., and Wang, Z. Q.: Arctic regional reanalysis on single levels from 1991 to present, https://doi.org/10.24381/cds.713858f6, accessed: 2026-01-26, 2020.

Stroeve, J., Nandan, V., Willatt, R., Tonboe, R., Hendricks, S., Ricker, R., Mead, J., Mallett, R., Huntemann, M., Itkin, P., Schneebeli, M., Krampe, D., Spreen, G., Wilkinson, J., Matero, I., Hoppmann, M., and Tsamados, M.: Surface-based Ku-and Ka-band polarimetric radar for sea ice studies, Cryosphere, 14, 4405–4426, https://doi.org/10.5194/TC-14-4405-2020, 2020.

Sturm, M. and Holmgren, J.: An Automatic Snow Depth Probe for Field Validation Campaigns, https://doi.org/10.1029/2018WR023559.

Sturm, M., Holmgren, J., Perovich, D. K., Holmgren, J., and Perovich, D. K.: Winter snow cover on the sea ice of the Arctic Ocean at the Surface Heat Budget of the Arctic Ocean (SHEBA): Temporal evolution and spatial variability, J. Geophys. Res, 107, 8047, https://doi.org/10.1029/2000JC000400, 1827.

Thompson, P., Hart, M., Livingstone, C., and Harvey, I.: SAMS SIMBA Instruction Manual, https://www.sams.ac.uk/t4-media/sams/pdf/SIMBA-Instruction-Manual.pdf, accessed: 2026-03-11, 2025.

Tonboe, R. T., Nandan, V., Yackel, J., Kern, S., Toudal Pedersen, L., and Stroeve, J.: Simulated Ka-and Ku-band radar altimeter height and freeboard estimation on snow-covered Arctic sea ice, Cryosphere, 15, 1811–1822, https://doi.org/10.5194/TC-15-1811-2021, 2021.

Ulaby, F. T., Moore, R. K., and Fung, A. K.: Microwave remote sensing: Active and passive. volume 1-microwave remote sensing fundamentals and radiometry, 1981.

Wadhams, P., Tucker, W. B., Krabill, W. B., Swift, R. N., Comiso, J. C., and Davis, N. R.: Relationship between sea ice freeboard and draft in the Arctic Basin, and implications for ice thickness monitoring, Journal of Geophysical Research, 97, https://doi.org/10.1029/92jc02014, 1992.

https://doi.org/10.5194/egusphere-2026-1662
Preprint. Discussion started: 26 March 2026

Willatt, R., Laxon, S., Giles, K., Cullen, R., Haas, C., and Helm, V.: Ku-band radar penetration into snow cover on Arctic sea ice using airborne data, Annals of Glaciology, 52, 197–205, https://doi.org/10.3189/172756411795931589, 2011.

Willatt, R., Stroeve, J. C., Nandan, V., Newman, T., Mallett, R., Hendricks, S., Ricker, R., Mead, J., Itkin, P., Tonboe, R., Wagner, D. N., Spreen, G., Liston, G., Schneebeli, M., Krampe, D., Tsamados, M., Demir, O., Wilkinson, J., Jaggi, M., Zhou, L., Huntemann, M., Raphael, I. A., Jutila, A., and Oggier, M.: Retrieval of Snow Depth on Arctic Sea Ice From Surface-Based, Polarimetric, Dual-Frequency Radar Altimetry, Geophysical Research Letters, 50, e2023GL104 461, https://doi.org/10.1029/2023GL104461, 2023.

Willatt, R., Mallett, R., Stroeve, J., Wilkinson, J., Nandan, V., and Newman, T.: Ku-and Ka-Band Polarimetric Radar Waveforms and Snow Depth Estimation Over Multi-Year Antarctic Sea Ice in the Weddell Sea, https://doi.org/10.1029/2024GL112870, 2025.

Wingham, D., Francis, C., Baker, S., Bouzinac, C., Brockley, D., Cullen, R., de Chateau-Thierry, P., Laxon, S., Mallow, U., Mavrocordatos, C., Phalippou, L., Ratier, G., Rey, L., Rostan, F., Viau, P., and Wallis, D.: CryoSat: A mission to determine the fluctuations in Earth's land and marine ice fields, Advances in Space Research, 37, 841–871, https://doi.org/https://doi.org/10.1016/j.asr.2005.07.027, natural Hazards and Oceanographic Processes from Satellite Data, 2006.

Yackel, J. J. and Barber, D. G.: Melt ponds on sea ice in the Canadian Archipelago: 2. On the use of RADARSAT-1 synthetic aperture radar for geophysical inversion, JOURNAL OF GEOPHYSICAL RESEARCH, 105, 61–83, https://doi.org/10.1029/2000JC900076, 2000.

Yackel, J. J., Barber, D. G., and Papakyriakou, T. N.: On the Estimation of Spring Melt in the North Water Polynya using RADARSAT-1, Tech. Rep. 3, 2001.

Zhou, L., Skourup, H., Stroeve, J., Kacimi, S., Arndt, S., Zhu, W., Petty, A., Huang, L., and Xu, S.: Snow effects on altimeter waveforms over sea ice in the Weddell Sea — Part I: Radar waveform decomposition, Remote Sensing of Environment, 333, https://doi.org/10.1016/J.RSE.2025.115112, 2026.

Zhu, W., Liu, S., Xu, S., and Zhou, L.: A 12-year climate record of wintertime wave-affected marginal ice zones in the Atlantic Arctic based on CryoSat-2, Earth Syst. Sci. Data, 16, https://doi.org/10.5194/essd-16-2917-2024, 2917.